This paper is accepted for publication in Geobiology
(https://onlinelibrary.wiley.com/journal/14724669)

A microbial role in the construction of Mono Lake carbonate chimneys?

Alex Brasier, School of Geosciences, University of Aberdeen
(a.brasier@abdn.ac.uk)

David Wacey, University of Western Australia

Mike Rogerson, University of Hull

Paul Guagliardo, University of Western Australia

Martin Saunders, University of Western Australia

Siri Kellner, University of Western Australia

Ramon Mercedes-Martin, University of Hull

Tim Prior, University of Hull

Colin Taylor, University of Aberdeen

Anna Matthews, BP Exploration

John Reijmer, KFUPM Saudi Arabia, and VU University Amsterdam

Running title: Mono Lake carbonate chimneys

ABSTRACT

Lacustrine carbonate chimneys are striking, metre-scale constructions. If these were bio-influenced constructions, they could be priority targets in the search for early and extraterrestrial microbial life. However, there are questions over whether such chimneys are built on a geobiological framework, or are solely abiotic geomorphological features produced by mixing of lake and spring waters. Here we use correlative microscopy to show that microbes were living around Pleistocene Mono Lake carbonate chimneys during their growth. A plausible interpretation, in line with some recent works by others on other lacustrine carbonates, is that benthic

This paper is accepted for publication in Geobiology
(https://onlinelibrary.wiley.com/journal/14724669)

cyanobacteria and their associated extracellular organic material (EOM) formed tubular biofilms around rising sub-lacustrine spring vent waters, binding calcium ions and trapping and binding detrital silicate sediment. Decay of these biofilms would locally have increased calcium and carbonate ion activity, inducing calcite precipitation on and around the biofilms. Early manganese carbonate mineralization was directly associated with cell walls, potentially related to microbial activity though the precise mechanism remains to be elucidated. Much of the calcite crystal growth was likely abiotic, and no strong evidence for either authigenic silicate growth or a clay mineral precursor framework was observed. Nevertheless it seems likely that the biofilms provided initial sites for calcite nucleation and encouraged the primary organized crystal growth. We suggest that the nano, micro and macro scale fabrics of these Pleistocene Mono Lake chimneys were affected by the presence of centimeter-thick tubular and vertically-stacked calcifying microbial mats. Such carbonate chimneys represent a promising macro-scale target in the exploration for ancient or extra-terrestrial life.

INTRODUCTION

Distinguishing biologically-influenced sedimentary rock structures from abiotic ones in the field, or when selecting high priority targets from remote images, is a key challenge in the search for early and extra-terrestrial life. There are few recognisable millimetre to decimetre-scale structures identifiable as definitively ‘microbial’ in outcrop. Free-standing chimneys composed of carbonate, sulphate or silicate minerals, if requiring the influence of organisms to develop, provide a potential set of targets for terrestrial geological and astrobiological investigation (e.g., Walter and Des Marais, 1993).

This paper is accepted for publication in Geobiology
(https://onlinelibrary.wiley.com/journal/14724669)

Mono Lake, California, is a globally important site for studying potential biogeochemical processes creating 'tufa' limestone chimney constructions around sub-lacustrine vents. It is renowned for its Pleistocene to 20th century vegetation-encrusting tufa, found aligned along faults associated with springs, and boulder-encrusting tufa sheets on the lake margins (Russell, 1889; Dunn, 1953). These impressive, tower-like structures are only the most recent phase of lacustrine carbonate deposition that has been occurring sporadically within Mono Lake at least since the last glaciation (Wang et al., 2014). Although together these features are considered an archetypal carbonate-precipitating hyperalkline lacustrine environment (Della Porta, 2015), their depositional mechanisms are surprisingly little studied. This is in part because no active carbonate mineral precipitation has been reported since sporadic events in the 1980s and early 1990s, when ikaite ($CaCO_3.6H_2O$) and gaylussite ($Na_2Ca(CO_3)_{2.5}H_2O$) were reportedly forming where spring waters mixed with lake waters along the southern shore of the lake (Stine, 1987; Bischoff et al., 1993).

Both geochemical and geobiological models have been put forward in an attempt to explain voluminous past tufa formation in Mono Lake. In the purely geochemically driven models, it is postulated that calcium carbonate precipitation was caused by mixing of carbonate-rich, high pH lake water with Ca-rich spring water (Dunn, 1953; Cloud and Lajoie, 1980; Rieger, 1992). Similar models have recently been invoked to help explain sublacustrine chimneys of the Afar Rift (Dekov et al., 2014). A popular geochemical model for Mono Lake contends that the dominant primary-formed carbonate mineralogy is ikaite (Bischoff et al., 1993), and that in most cases this later

recrystallizes to gaylussite (Bischoff et al., 1993) or calcite (Council and Bennett, 1993). Mound and chimney morphologies in these geochemical models are explained by mineral precipitation from upward rising, low-density sub-lacustrine plumes of spring waters. However, such chimneys have not actually been demonstrated to spontaneously form under sterile conditions, and turbulent mixing zones between water masses may produce powder-like mineral precipitates in the water column (consistent with the 'milky white' spring waters observed by Stine, 1987) rather than coherent benthic constructions. Macro-crystalline, benthic sheets of calcite in other contexts require the presence of a benthic biofilm (cf. Pedley et al., 2009).

Early geobiological models were based on observations of microbes or algae at sites of active tufa growth that were inferred to have influenced carbonate precipitation (Scholl and Taft, 1964). Given the enormous dissolved inorganic carbon (DIC) pool in Mono Lake and high pH such that the majority of this DIC is present as carbonate, postulated photosynthetic effects on carbonate mineral deposition are likely to be negligible (cf. Arp et al., 2001). Stable carbon isotopes of Mono Lake tufa samples record temporal variations in the bulk lake water DIC that relate to changes in plankton productivity and burial (Li and Ku, 1997). However, no study has yet reported any local $\delta^{13}C_{calcite}$ enrichment relative to lake average that could be attributed to photosynthetic CO_2 uptake at the site of carbonate precipitation. Instead, a more logical microbial mechanism for carbonate mineral formation is via binding of calcium by the copious amounts of extra-cellular organic material (EOM) produced by cyanobacteria (Emeis et al., 1987), with calcification taking place during or following calcium release on heterotrophic EOM breakdown (Arp et al., 1998; 1999; 2001; Dupraz et al., 2004). We follow others including Dupraz et al. (2013) in using

the broader term EOM rather than EPS (extracellular polymeric substances) here because EOM encompasses all organic matter external to the cell, including low molecular weight organic carbon, not just the larger EPS molecules.

An alternative geobiological model for carbonate chimney growth in Mono Lake might be calcite replacement of a microbially-precipitated clay precursor, as has been proposed for thrombolitic microbial carbonates of Lake Clifton, Australia (Burne et al., 2014) and dolomitic microbialites of Great Salt Lake, USA (Pace et al., 2016). Pertinent to this model was a report of potential microbial mediation of magnesium silicate growth within calcite-cemented clastic lake sediment (locally known as 'sand tufa'; Cloud and Lajoie, 1980) on the southern shore of Mono Lake (Souza-Egipsy et al., 2005). In these lake sands, however, no evidence for calcite precipitation around living or decaying microbes was found (Souza-Egipsy et al., 2005).

Geomorphologically, mound and column structures are well known to arise under the influence of photosynthetic (cf. stromatolites and thrombolites) and chemosynthetic (black and white smoker) microbial activity, with the biofilm providing a focus for mineral growth and directly promoting benthic carbonate mineral sheet formation (Kempe et al., 1991; Reid, et al., 2000; Bosak et al., 2012; Petroff et al., 2013). Here we provide new *in situ* macro- to nano-scale evidence for the participation of microbes in the construction of Mono Lake chimneys, and argue that the location and morphology of the Mono Lake tufa chimneys is a result of a complex interplay between lake dynamics (faults, venting of sub-lacustrine springs, lake chemistry) and the benthic microbial communities within the lake.

This paper is accepted for publication in Geobiology
(https://onlinelibrary.wiley.com/journal/14724669)

METHODS

Fieldwork and sample processing

Fieldwork around Mono Lake was undertaken in October 2014. Samples were taken with permission of the Mono Lake State Natural Tufa Reserve following their guidelines and under their supervision. It was a requirement of the permit that only the minimum required number of naturally broken samples should be taken. Several different occurrences of tufa carbonate rocks were examined around the lake, but the most interesting were Pleistocene chimney structures close to Mono City (Fig. 1, Fig. 2A) that are the focus of this article. Possible microbial influence on construction of these chimneys was noted in the field (Fig. 2), based on mat-like sheets that connected chimney pipes (Fig. 2B). The locations of the chimneys as determined by GPS are linearly arranged, presumably along a fault. Indeed faults mapped by Jennings et al. (1977) run parallel to the line of the Pleistocene chimneys (Fig. 1). Further laboratory work was aimed at determining whether the central chimney pipes were solely abiotic or microbially influenced in origin. For this, a representative (naturally broken) sample that was clearly from the centre of a chimney was sent to VU University Amsterdam. Pipe material was cut up and pieces were consolidated by impregnation with blue-stained epoxy resin so that several thin-sections could be made. Very high abundance of organic filaments was apparent in each of these pipe wall thin-sections (described and illustrated further below). A large number (>10) of thin sections of this pipe material were optically examined and then sent to the Centre for Microscopy, Characterisation and Analysis at the University of Western Australia. One representative thin-section was selected for NanoSIMS, FIB-SEM and TEM analyses to test (1) whether the filaments were genuine microfossils, and (2) to determine

spatial relationships between cell walls and minerals, which might help to determine whether these purported microbes influenced chimney growth form.

XRD analysis

Three sub-samples of the same specimen from which the thin-sections were produced were crushed for XRD analysis at the University of Hull. X-ray powder diffraction data were collected from ground samples mounted in stainless steel sample holders. Analysis was performed on a PANAlytical Empyrean X-ray diffractometer (XRD) operating in Bragg-Brentano geometry using copper $K\alpha_1$ radiation (λ = 1.540546 Å), and a PIXEL detector. Each data set was the sum of three identical data collections with $4 \leq 2\theta\ /° \leq 100$, a step size of 0.02626 °, and counting time 1140 s per step.

Biomarker analysis

Biomarker analysis was conducted on a further off-cut of the Pleistocene tufa chimney specimen used for XRD analysis and microscopy. This was done in the organic geochemistry laboratory at the University of Aberdeen. The sample was first cleaned with Dichloromethane. It was then crushed and Soxhlet extracted using a Dichloromethane/Methanol mixture (93:7). The extract was analysed on an Agilent 6890GC with an Agilent 5975MS. The GC column was a 30m long * 0.25mm i.d. * 0.25um film thickness GC-5 column. The gas chromatography temperature programme was 60°C for 2 minutes, heating at 20°C per minute up to 120°C, then at 4°C per minute up to 290°C, and holding for 27.5 minutes.

Focussed ion beam (FIB) preparation of TEM samples

Prior to FIB preparation, resin-embedded polished geological thin sections were examined by optical microscopy, using *Zeiss Axioskop 2 and Leica DM2500M* microscopes, plus scanning electron microscopy (SEM), using a *FEI Verios XHR* SEM, in order to gain an understanding of filament distributions and morphologies, and to select the most appropriate targets for detailed study. A dual-beam FIB system (*FEI Helios NanoLab G3 CX*) at the Centre for Microscopy, Characterisation and Analysis, University of Western Australia, was then used to prepare ultrathin TEM wafers from the thin sections coated with c. 20 nm of gold. Electron beam imaging within the dual beam FIB was used to identify previously mapped microstructures of interest in the thin sections allowing site-specific TEM samples to be prepared. The TEM sections were prepared by a series of steps involving different ion beam energies and currents (see Wacey et al., 2011 for details); after initial thinning to c. 1 μm the wafers were extracted using an *in-situ* micromanipulator and welded onto *PELCO* FIB-lift-out Cu TEM grids. Final thinning to c. 150 nm was then done *in situ* on the grid using lower beam currents. FIB preparation of TEM sections allows features below the surface of the thin sections to be targeted, thus eliminating the risk of surface contamination producing artefacts. Distinction between the epoxy resin used in sample preparation and other organic materials was possible via NanoSIMS ion mapping (see below).

TEM analysis of FIB-milled wafers

TEM data were obtained using a *FEI Titan G2 80-200* TEM/STEM with *ChemiSTEM Technology* operating at 200 kV, located within the Centre for Microscopy, Characterisation and Analysis, University of Western Australia. Data obtained included bright-field TEM images, HAADF (high angle annular dark-field) STEM

images, EDS (*ChemiSTEM*) maps, and selected area electron diffraction patterns for mineral identification.

SEM-EDS

SEM-EDS was performed on the *FEI Helios Nanolab G3 CX* instrument at the Centre for Microscopy, Characterisation and Analysis, University of Western Australia which is equipped with an *Oxford Instruments X-Max 80* energy dispersive X-ray spectroscopy (EDS) system and *Oxford Instruments AZtec 3.0* nano-analysis software. All analyses were performed on FIB-milled faces below and perpendicular to the surface of the thin sections to avoid surface contamination.

NanoSIMS ion mapping

NanoSIMS ion mapping was performed using a *CAMECA NanoSIMS 50* at the Centre for Microscopy, Characterisation and Analysis, University of Western Australia, with instrument parameters optimized as described in Wacey et al., 2011. Analysis areas varied from 22 x 22 μm up to 35 x 35 μm, at a resolution of 256 x 256 pixels (each pixel measuring between 86 nm and 137 nm, depending on the size of the area imaged). Dwell times were 30 ms per pixel with a beam current of c. 1.3 pA (D1=3). Secondary ions mapped were $^{16}O^-$, $^{24}C_2^-$, $^{12}C^{14}N^-$, $^{28}Si^-$, $^{24}Mg^{16}O^-$ and $^{56}Fe^{16}O^-$, and charge compensation was achieved by using the electron flood gun. In all cases, regions c. 2-5 μm larger than the intended analysis area were pre-sputtered with the primary ion beam (using c. 17 pA beam current; D1=1) to > 5 x 10^{16} ions/cm^2 in order to remove surface contamination, implant Cs^+ ions and reach a steady-state of ion emission. NanoSIMS data presented were produced in one session, but to enable measurement of six different ions with the *CAMECA NanoSIMS 50* each

area was analysed twice, with one detector retuned between analyses. For each area, analysis one was O, C, CN, Si, FeO, and analysis two was O, C, CN, MgO, FeO. Differences in the relative intensities of the $^{24}C_2^-$ versus $^{12}C^{14}N^-$ maps are partly due to the higher ionization potential of the secondary ion $^{12}C^{14}N^-$; here we report only the $^{12}C^{14}N^-$ maps because of the higher secondary ion yield and the fact that $^{24}C_2^-$ is also found in the carbonate minerals surrounding the organic material. $^{12}C^{14}N^-/^{24}C_2^-$ ratios were used to identify epoxy resin introduced during sample preparation based on previous data showing that the epoxy possesses significantly lower $^{12}C^{14}N^-/^{24}C_2^-$ than that of biological cell walls or potential extracellular organic material (Wacey et al., 2010).

RESULTS

Our study aimed to determine whether Mono Lake chimneys are purely physico-chemical constructions, or whether microbes influenced their development. We focus on chimneys found north of the present lake at Mono City, on a Pleistocene lake terrace (Zimmerman et al., 2011) at around 2065 m altitude, extending along a 2.25 km long N to NNE oriented line interpreted as a fault trace (Fig. 1). Latitudes and longitudes of the studied chimneys are provided as supplementary information. The late Pleistocene Mono City chimneys reported and described here are older than the more commonly studied and illustrated mounds of presumed Holocene and younger age found close to the modern shoreline in the south east (South Tufa) and north east (Boardwalk area) of the lake (Fig. 1). A sample of a Holocene fallen block from the Lee Vining area on the southwest shore of the modern lake was also analysed by XRD for comparison to the Pleistocene materials.

The Mono City chimneys vary from c.3 to 4 m in height, and from c. 1.5 to 3 m in width (Fig. 2A). Internally the chimneys are constructed of stacks of numerous calcitic cones or pipes, each 30 to 60 cm in height and around 3 cm in width (Figs. 2A-C). Each pipe has a central 1 cm-sized void or conduit (Figs. 2B, 3A, 3B). The outsides of these pipes are commonly coated in botryoids of calcite (confirmed by XRD) that range from 0.5 to 3 cm across (Fig. 2C). Sub-horizontal 15 cm-thick laminated calcitic sheets were observed between the pipes, binding them together (Fig. 2B). Each chimney was found rooted in calcite-cemented lake sediment ('sand tufa'). Externally, the chimneys were encrusted in 20 to 50 cm thick blankets of centimetre-scale mesh-like networks of euhedral pseudomorphs after the low temperature hydrated $CaCO_3$ mineral ikaite, locally known as 'thinolite tufa' (Russell, 1889; Shearman et al., 1989) (Figs. 2A, 2D). Some of these pseudomorphs after ikaite are found on individual pipes that make up the chimneys, but only on outer pipe surfaces, which would have been exposed to lake water after the chimney had formed. Individual pseudomorphs of ikaite crystals in these 'thinolite' blankets mostly measured around 5 cm in length, and crystals clustered together to form rosettes (Fig. 2D).

Petrography of chimney pipes

The walls of the c. 3 cm wide chimney pipes are mostly 0.5 to 1 cm thick, constructed of columns of calcite that grew radially around the c. 1 cm wide central conduit (Fig. 3A-C). In places the calcite crystal columns that make up the pipe walls were cemented together, particularly towards the outside of the pipes. In zones closer to pipe conduits, however, the microsparry calcite columns were separated from each other by elongated voids running parallel to the column long axis (Fig. 3A-B). Calcite

crystal microspar columns may also branch and fan outwards resulting in millimetre to centimetre scale shrub-like morphologies (Fig. 3D). When cut perpendicular to the crystal growth axes these radiating calcite fans appeared sub-circular. Between some of the pipes, fissure fills of clastic sediment were present.

Microfossils within chimney pipes

Clusters of filaments, observed in thin-sections under the optical microscope, are a major component of the chimneys: they are ubiquitous within the columnar to shrub-like calcite growths that make up the pipe walls (Fig. 4A-C), with many thousands of specimens in a single thin section. Many of these filamentous structures were found rather randomly oriented, though others were oriented approximately perpendicular to outward-radiating sub-crystal boundaries (Fig. 4C).

Filaments may be divided into two main types, found together in the same thin-sections, occupying the same niche. The most common (Type 1) have diameters in the range of c. 0.8 to 8 μm with modal peaks at c. 1 μm and c. 2.5 μm ($n > 500$) (Fig. 4D, E, H). Type 1 filaments tend to be dark in colour, suggesting high organic content and poorly mineralised interiors. The Type 1 assemblage is dominated by empty sheaths (Fig. 4A, H), although occasionally trichomes, some with putative segmentation, can be recognised (Fig. 4D). Type 2 filaments have diameters in the range of c. 10 to 14.5 μm ($n > 100$), and comprise well-preserved trichomes with clear interior mineralisation. Trichome segmentation is present in almost all cases (Fig. 4B, E-G) and potential remains of cell contents are sometimes observed (Fig. 4G). Type 2 filament sheaths are either completely mineralised or were absent. Coccoids were also identified, ranging from 6.8 to 15 μm diameter ($n = 25$), but these were much rarer

311 than filaments in the thin-sections examined (Fig. 4I). The morphologies of the
312 filaments, including their size, segmentation, and cases of trichomes inside sheaths,
313 are consistent with their being fossils of cyanobacteria, as are found within modern
314 Mono Lake spring systems (Kulp et al., 2008). Biomarker data reinforces this
315 interpretation (see below and Fig. 5). The microfossils are almost all in the inclusion-
316 rich calcite of the chimney pipe walls, being rare to absent in the optically transparent
317 calcitic pseudomorph after ikaite overgrowths of the thinolite blanket (Fig. 3E).
318
319 **Tufa and microfossil chemistry**
320 Bulk rock mineralogy was determined by XRD, with GC-MS for biomarkers of
321 organic carbon entombed within the rock. The chemistry and ultrastructure of the
322 filamentous microfossils and surrounding minerals were further investigated using a
323 combination of nano-scale secondary ion mass spectrometry (NanoSIMS), scanning
324 electron microscopy (SEM) and transmission electron microscopy (TEM).
325
326 The XRD data showed ~99% of chimney pipe rock to be calcite with an average
327 magnesium content of 8.1(1) %. The remaining ~1% constituent of the rock was
328 quartz (Fig. S1A-C). The Pleistocene Mono City chimneys are therefore significantly
329 different in mineralogy from the younger, aragonitic, Holocene tufa mounds (Fig.
330 S1D).
331
332 The hydrocarbon lipids obtained from a solvent extract of the Mono City chimney
333 specimen (Fig. 5) are similar to those of Arp et al. (1999) reported for Pyramid Lake
334 and also to those found in endolithic and mat-forming cyanobacteria reported by
335 Parnell et al. (2007). Typical features found in these stressed environments include a

predominance of *n*-C_{15} to C_{18} *n*-alkanes with a maximum at C_{17}, plus abundant monomethylalkanes and hydrocarbon hopenes such as diploptene (Fig. 5). More generally it has been known for some time (Han et al. 1968; Thiel et al. 1997) that abundant *n*-C_{17} and monomethlyalkanes (Shiea, 1990), can be found in photosynthetic cyanobacteria. This is entirely consistent with the specimen petrography.

Filaments identified in the chimney pipe wall thin-sections are highlighted particularly well in carbon and nitrogen NanoSIMS ion maps, with trichome segmentation in Type 2 filaments notable in several cases (Fig. 6). Carbon and nitrogen are also frequently found with a very patchy distribution in places outside the trichomes (Figs. 6-9) and are here interpreted as degraded extracellular organic material (EOM) from cyanobacterial sheaths and biofilms. This preserved 'EOM' can be distinguished in the NanoSIMS data from potential epoxy resin contamination as the latter lacks nitrogen, so its $^{12}C^{14}N^{-}/^{24}C_2^{-}$ ratio is significantly less than the $^{12}C^{14}N^{-}/^{24}C_2^{-}$ ratios for cell walls or potential EOM (Fig. S2). Alternatively this organic carbon could be interpreted as escaped cell contents or degrading cell walls, but an EOM interpretation is the most parsimonious explanation. NanoSIMS, SEM-EDS and TEM-EDS maps of Si show abundant silicate nanograins surrounding many of the Type 1 and Type 2 filaments, spatially associated with the C and N (detected by NanoSIMS and/or TEM) that can be interpreted as fossilised EOM (Fig. 6B-C, E-F, H-I; Fig. 7C, I-L; Fig. 8B; Fig 9). These silicates have rather variable compositions and include (in order of abundance) quartz, K-Na-rich aluminosilicate (cf. alkali feldspar), plus Fe and Mg rich aluminosilicates (cf. chlorite group) (Fig. 8-9). Silicates were only exceptionally rarely found in the interior of the filaments, and in these few cases they were very close to the cell wall. In most observed cases

filament interiors were filled solely with calcite. In one examined Type 2 filament, a Mn-Fe-rich carbonate mineral was observed within and just exterior to a cell wall (Fig. 7A, E-F), while in one examined Type 1 filament a Mn-Ti-Fe-rich carbonate was observed partially replacing the filament wall (Fig. 9).

A rare sub-population of Si-rich grains were found in close association with organic cell wall material; these comprise SiC and are laboratory contamination, having been introduced during polishing of the thin sections. These can easily be discriminated from true silicate minerals by their characteristic Si and C chemistry and lack of other elements (e.g., O) found in silicate minerals (Fig. 6, white grains), and have been eliminated from further discussions.

3D microfossil morphology and mineral distribution

A three-dimensional reconstructions of a Type 2 fossil filament was produced from stacked SEM-BSE images captured during sequential focussed ion beam milling (see materials and methods). The reconstruction, correlated with SEM-EDS and NanoSIMS ion maps, reveals carbonaceous cell walls and cell dividing cross walls of a filamentous cyanobacterium (Fig. 7A-C, black; Fig. 7D-L, brown). Some internal cell contents are remarkably fossilised, preserved as organic carbon structures encased in calcite (Fig. 7D-L, green). The reconstruction emphasises that the interior of the cells are preserved entirely in calcite and lack inclusions of other grains. In one region an external cell wall is directly associated with an Mn-Fe-rich carbonate mineral (Fig. 7E-F, H-L, blue). Silicate minerals are again shown to be spatially associated with partially degraded EOM surrounding the cells (Fig. 7C, I-L, silicates in purple, EOM in yellow).

This paper is accepted for publication in Geobiology
(https://onlinelibrary.wiley.com/journal/14724669)

DISCUSSION

Temporal environmental changes

Some aspects of the chimneys appear to be entirely abiotic in origin: for example, the thinolite around the outside of the chimney and in places on the outsides of the central pipes very likely formed via recrystallization of ikaite to calcite. This process is accompanied by a significant volume decrease, explaining the extreme porosity of the mesh-like thinolite networks (Shearman et al., 1989). That the ikaite formed a blanket covering of the chimneys suggests a change in environmental conditions, probably including a drop in lake water temperature, at some time following chimney development (Shearman et al., 1989). Suggestions of temporal environmental changes affecting carbonate mineral fabric are entirely consistent with the early observations of Russell (1889) who first noted that thinolite was only found at higher elevations around the lake.

A further environmental change is apparent in our new data: the dominance of high-Mg calcite within the Pleistocene deposits of the Mono City chimneys contrasts with aragonite (Fig. S1) and Mg-silicate (Souza-Egipsy et al., 2005) mineralogy of the younger Holocene mounds. Unfortunately, it is not possible for us to conclusively demonstrate co-occurrence of Mg-Si phases and aragonite because the samples we analysed were free of this material, and Souza-Egipsy et al (2005) did not present crystallographic data. Rather, they assumed that Ca, O, C phases identified by EDS were low-Mg calcite: it seems likely that this was in fact aragonite. Calcite solubility is known to increase as fluid Mg/Ca ratios are raised (Davis et al., 2000), such that rising Mg/Ca in the lake water sometime after the Mono City chimneys had formed

could itself cause a change in the precipitating carbonate mineral from Pleistocene calcite to Holocene aragonite. Mg/Ca in spring and runoff waters within the Mono region range from 0.04 to 1, whereas lake waters are always >1 (Table 1) indicating that Ca is consumed selectively over Mg. This scavenging of Ca will be inversely proportional to the alkalinity (due to combined influence on the saturation product), and therefore likely inversely proportional to the lake level via dilution. Enhanced scavenging of Ca relative to Mg during lake lowstands will raise Mg/Ca during these time intervals, favouring aragonite precipitation. Reduced incorporation of Mg into aragonite due to very low $D_{Mg\text{-}aragonite}$ (Wassenburg et al., 2016) will cause a further rise in the lake water Mg concentration, ultimately triggering precipitation of non-carbonate Mg phases alongside aragonite. Hence, highstand high-Mg calcite deposition and lowstand aragonite + Mg-silicate precipitation can be seen as an inherent, thermodynamically controlled behaviour of Mono Lake, and similar hyper-alkaline systems.

In contrast to the outer thinolite blanket, there is no petrographic evidence of any recrystallization of the Pleistocene calcitic chimney pipe walls (Fig. 3). It is in these un-recrystallised and earlier formed calcite pipe walls that filamentous inclusions are found.

Inclusions in the calcite

Biomarkers, NanoSIMS, SEM- and TEM-EDS elemental maps show the filamentous structures examined in pipe walls are clearly carbonaceous microfossils, while these techniques combined with light microscopy observations, together show the detailed

spatial relationships between these fossil cyanobacterial filaments and calcite and silicate minerals.

Several mechanisms are plausible to explain the observed arrangement of silicates around filaments. First is an abiotic hypothesis, in which the microbes had no effect on silicate mineral distribution. However, here we might expect that any partially decayed cells would contain silicate grains that had been washed inside, and this was not observed. Rather, it seems that the organic matter that we interpret as cell walls and EOM was spatially linked to the locations of the silicate grains (e.g., Fig. 7). This leaves us with two hypotheses to assess: 1) that silicates could have been precipitated *in situ* via the metabolic activity of microbes (cf. Burne et al., 2014); or 2) they could be fine detrital grains that have been trapped and bound by microbial EOM (cf. Reid et al., 2000).

Microbial precipitation of silicate precursors versus detrital silicate grains

Authigenic microbial precipitation of silicates has recently been reported in a number of alkaline lakes (e.g., Lake Satonda (Arp et al., 2003); Lake Clifton (Caselmann, 2005; Burne et al., 2014); Mexican Crater Lakes (Zeyen et al., 2015); Great Salt Lake (Pace et al., 2016); Lake Thetis (Caselmann, 2005; Wacey et al., 2017)), where it has been suggested that local increases of pH during oxygenic photosynthesis favour the precipitation of Mg-Si phases in and around cyanobacterial sheaths and in webs of EOM (e.g., Pace et al., 2016). In this scenario, carbonate minerals only precipitate (and often replace Mg-Si phases) at a later stage when the activities of CO_3 and Ca rise during heterotrophic degradation of cyanobacteria and their associated EOM. However, the chemistry and distribution of silicates in those aforementioned lake

460 deposits are rather different to that observed in the calcitic Pleistocene Mono City
461 chimneys. Electron diffraction patterns of individual silicates around the Mono City
462 chimney filaments revealed compositions compatible with chlorite and feldspar (Fig.
463 9), while bulk-rock XRD also indicates minor quartz (Fig. S1). Few of the silicate
464 grains examined contained abundant magnesium and none were pure Mg-Si phases
465 such as the stevensite and kerolite phases previously reported from other alkaline
466 lakes (Burne et al., 2014; Zeyen et al., 2015). Intriguingly, the lack of Mg-Si phases
467 around the Pleistocene Mono chimney microbes is a notable difference from Mg-Si
468 mineralised EOM reported from sand-cementing tufa of the modern Mono Lake
469 shoreline (Souza-Egipsy et al., 2005).
470
471 It seems most likely that most if not all of the Pleistocene Mono City chimney
472 silicates were detrital grains. In support of this interpretation, we note that many
473 containedAl, which is often cited to indicate a detrital sediment component (e.g.,
474 Koning et al., 2002), and alkali feldspars cannot have formed *in situ* under lakewater
475 pressures. Furthermore, the very patchy isolated pattern of grain distribution and their
476 angular shapes (Figs. 6, 8-9) are in stark contrast to the generally massive nature of
477 Mg-Si precipitates found replicating entire cyanobacterial sheaths or large volumes of
478 thrombolites (Caselmann, 2005; Burne et al., 2014; Wacey et al., 2017) in other
479 alkaline lakes such as Lake Clifton and Lake Thetis in Western Australia.
480
481 While some authigenic chemical control of silicate precipitation by microbes, for
482 example by attraction of cations including Al, K and Si to negatively charged
483 compounds including uronic acids within the EOM (cf. Drews and Weckesser, 1982;
484 Saunders et al., 2014), cannot be ruled out, the mechanism that best explains the

morphologies, compositions and distribution of silicates in the Mono Lake chimneys is via trapping and binding by microbial EOM (cf. Reid et al., 2000).

In summary, there is no clear evidence that the individual and rather isolated silicate grains surrounding cyanobacterial filaments in the Mono Lake chimneys once formed a substantial and coherent template that could have acted as a precursor to the carbonate that is the dominant chimney constituent. That exceptionally preserved fossil microbial filaments are found in chimney calcite that is Mg-Si poor demonstrates that precursor silicate matrices are not prerequisites for cellular preservation of microbial life in alkaline lakes. Rather, formation of calcite in the Pleistocene Mono Lake (and elsewhere?) instead of coupled aragonite and amorphous Mg-Si phases seen in the Holocene Mono Lake mounds may dominantly reflect lower Mg/Ca ratios of the precipitating lake waters. Rising water levels in Mono Lake resulting in falling Mg/Ca ratios would likely cause the system to revert to precipitation of calcite, rather than aragonite and amorphous Mg-silicates.

Intracellular carbonate minerals

Carbonate minerals dominate the pipes making up the Mono Lake chimneys and on the microscale are found both intracellularly and extracellularly in the examined groups of filamentous microfossils. Intracellular calcification of cyanobacteria was recently described from modern lacustrine microbialites of Lake Alchichica, Mexico (Couradeau et al., 2012). This took the form of spherical granules of benstonite $(Sr_1Ba_{2.7}Mg_{1.4}C_{10.9})Ca_6Mg(CO_3)_{13}$, averaging 270 nm in diameter that may have nucleated on carboxysomes. The authors of that study suggested that excess alkalinity produced during photosynthesis was trapped inside the cell by active precipitation of

benstonite and not exported beyond the cell wall. However, the mineral fill of the fossil cyanobacteria of Mono Lake is calcite, which is neither rich in barium nor strontium, and no evidence for spherical granules was observed. There is some evidence of cell contents preserved within the cyanobacteria (Fig. 7) but this takes the form of patchy degraded organic material and this likely represents the least labile intracellular material. The cause(s) and timing of carbonate mineral growth within such cells remains to be elucidated, though here could simply have been post-mortem infiltration of the cell by a calcite-supersaturated fluid.

Manganese (+/- Fe and Ti) carbonate is rare but when present is an amorphous phase based on electron diffraction, and distinctly associated with the cell wall itself (Fig. 7A, Fig. 9). This was true of both Type 1 and Type 2 filaments. Bacterial cell walls are known to selectively accumulate Mn from surface waters (Konhauser et al., 1993). Association of Mn with the cell wall and not just the EOM suggests the mineralisation process involved more than a simple attraction of Mn cations to a negatively charged surface. The difference in Eh-pH conditions between the inside of the cell and mixed vent and lake waters outside the cell wall could explain this, as Mn^{2+} would be soluble inside the relatively low pH cell, but Mn carbonates would precipitate out at the redox boundary with high pH lake conditions (cf. Davison, 1993). This suggests that the rather rare Mn carbonates could have formed early.

Biological influences on chimney growth

The majority of the calcite that makes up the chimneys developed outside the microbial filaments. By binding calcium the EOM will initially have inhibited calcite crystal formation, but on degradation this calcium will have been released (cf. Arp et

al., 1999; 2001), and critically, tubular sheets of EOM from microbes that inhabited the zones around the rising vent waters will have been preferential sites of calcite crystal nucleation. Once calcite crystals had formed in the EOM of these mucilaginous, cohesive and quickly mineralised tubular sheets, there would be a lower activation energy to deposit more mass on these developing crystals than to generate new nuclei in the mixing water masses. Consequently, even if further chimney wall crystal growth operated via a largely abiotic process, this latter deposition could still be considered bio-influenced due to the control on location from the presence of biofilm. It is tempting to speculate that the chimney form owes its origins in part to the presence of a biofilm. The rising chimney would present a stable substrate for microbial colonisation around likely the nutrient-rich (Table 1) and relatively well illuminated waters. The result could be that tubular biofilm growth around rising spring waters leads to the formation of carbonate chimney pipes, and in turn chimney growth assists biofilm development around the rising spring waters. Hence, the Mono City calcitic lacustrine chimneys seem broadly similar to other lacustrine hot-spring carbonates (Arp et al., 1999), volcanic crater lake carbonates (Arp et al., 2003; 2012; Kazmierczak et al., 2011), tufa barrages (Emeis et al., 1987), chimney-like giant (40 m high) aragonitic microbialites of Lake Van (Kempe et al., 1991), simpler structured carbonate mounds of other alkaline lakes like those of Inner Mongolia (Arp et al., 1998) and the Ries Crater, Germany (Pache et al,, 2001), as well as siliceous lacustrine hydrothermal chimneys like those of Lake Taupo, New Zealand (Jones et al., 2007) in that the *location* of the calcitic chimneys has a primary abiotic control (fault controlled rising spring waters), but chimney *morphology* may well be microbially mediated. Calcitic tufa chimney systems could therefore be added to the

list of macroscale products of local environmental chemistry, physics and microbiology, with the biota exerting a strong control on fabric.

Support for microbial mediation of tufa chimneys comes from simpler structured tufa mounds like those of nearby Pyramid Lake (Arp et al., 1999b) and Searle's Lake, California (Guo and Chafetz, 2012), where the mounds contain a macroscopic columnar stromatolite component plus microscopic calcite cemented spheres, chains of beads, rods, and filaments that strongly resemble bacteria (Guo and Chafetz, 2012). These observations led Guo and Chafetz (2012) to conclude that microbially induced calcification was the predominant process creating these deposits but they were unable to demonstrate a role for EOM. Similar observations come from the alkaline Lake Alchichica in Mexico where tubular chimney-like carbonate deposits (with central conduits similar to the Mono Lake material described herein) occur side-by-side with nodular and domal structures, all of which were interpreted as microbialites, with some preserving remnants of filamentous and coccoid cyanobacteria (Kazmierczak et al., 2011). These authors inferred that primary carbonate mineralization was nucleated within EOM secreted by cyanobacterial biofilms.

CONCLUSIONS

Summary model for chimney growth

Our results show that the Mono City chimney pipes are packed full of fossil microbial filaments, with rare coccoids. These might be interpreted as centimetre-thick tubular ("rolled up") and vertically stacked calcified microbial mats. Evidently there was strong growth of a cyanobacterial biofilm around rising spring waters in the Pleistocene Mono Lake, and these microbes influenced tufa chimney fabric

development at least at the nano- and microscales. Just exterior to the preserved microbial cells, quartz and aluminosilicate grains are best taken as evidence that 'sticky' EOM produced by cyanobacteria (and potentially other microbes) trapped and bound some clastic lake sediment grains. We cannot rule out that some of the aluminosilicates surrounding these filaments could have formed authigenically within the EOM (cf. Pace et al., 2016), although the chemistry of these grains, together with their angular shapes and isolated context in which several grains 'float' in a calcite matrix, indicates these silicate grains are mostly detrital. A key finding is that Mg-Si phases were absent here, so this phase cannot be seen as a prerequisite for exquisite fossilisation of microbes in alkaline water settings (cf Souza-Egipsy et al., 2005; Burne et al., 2014). Instead it seems likely that the calcitic nature of these Pleistocene chimneys reflects a low lake water Mg/Ca ratio, arising from dilution during phases of high lake level. Holocene aragonitic mounds coupled to Mg-Si phases (Souza-Egipsy et al., 2005) can then be explained by a rise in the lake water Mg/Ca ratio through time, and are a predictable feature of the thermodynamics of this lake and any similar system.

Fossilisation of the microbes was likely related to the microbial EOM (cf. Arp et al., 1999) in that acidic extracellular substances will have stripped calcium from the rising vent waters, favouring calcite nucleation and subsequent organised calcite crystal growth at the vent site. Calcite mineralisation of the EOM and intracellular calcification were likely *post-mortem* processes (cf. Arp et al., 2001, 2012). Adsorption of Mn to the organic carbon of the cell wall could also have happened *post-mortem*, but petrography suggests this was an early process.

Summation of the evidence shows Pleistocene fossil tufa chimneys of Mono Lake are not solely the result of abiotic mixing between calcium-rich spring waters and alkaline lake waters (cf. Council and Bennet, 1993), although they were arranged linearly along an apparent fault line, showing that water chemistry and tectonics controlled chimney locations if not their fabrics. Rather, chimney fabric development was influenced at least at the nano- to micro-scales by microbes that colonised the fertile and relatively nutrient-rich vent sites. These findings have direct applicability to the search for ancient and extraterrestrial microbial life.

ACKNOWLEDGEMENTS

Fieldwork was undertaken and samples collected under permit from CA State Parks collection and with the kind support of Mono Lake Tufa State Natural Reserve and the Mono Lake Committee. We acknowledge the facilities, scientific and technical assistance of the Australian Microscopy & Microanalysis Research Facility at the Centre for Microscopy Characterisation and Analysis, The University of Western Australia, a facility funded by the University, State and Commonwealth Governments. DW acknowledges funding from the Australian Research Council via the Future Fellowship scheme (FT140100321). BP Exploration Co. (GPTLlBPXlMB/NB/89573) is thanked for funding provided to the Universities of Hull and VU Amsterdam. SK acknowledges funding from the DAAD RISE internship programme. Three anonymous reviewers provided very helpful comments, which improved the final manuscript. The authors declare no conflicts of interest.

This paper is accepted for publication in Geobiology
(https://onlinelibrary.wiley.com/journal/14724669)

REFERENCES

Arp G, Helms G, Karlinska K, Schumann G, Reimer A, Reitner J, Trichet J (2012) Photosynthesis versus exopolymer degradation in the formation of microbialites on the atoll of Kirimati, Republic of Kiribati, Central Pacific. *Geomicrobiology Journal* **29**, 29-65.

Arp G, Reimer A, Reitner J (2003) Microbialite formation in seawater of increased alkalinity, Satonda Crater Lake, Indonesia. *Journal of Sedimentary Research* **73**, 105-127.

Arp G, Reimer A, Reitner J (2001) Photosynthesis-induced biofilm calcification and calcium concentrations in Phanerozoic oceans. *Science* **292**, 1701-1704.

Arp G, Thiel V, Reimer A, Michaelis W, Reitner J (1999) Biofilm exopolymers control microbialite formation at thermal springs discharging into the alkaline Pyramid Lake, Nevada, USA. *Sedimentary Geology* **126**, 159-176.

Arp G, Hofmann J, Reitner J (1998) Microbial Fabric Formation in Spring Mounds ("Microbialites") of Alkaline Salt Lakes in the Badain Jaran Sand Sea, PR China. *Palaios* **13**, 581-592.

Bischoff JL, Stine S, Rosenbauer RJ, Fitzpatrick JA, Stafford Jr TW (1993) Ikaite precipitation by mixing of shoreline springs and lake water, Mono Lake, California, USA. *Geochimica et Cosmochimica Acta* **57**, 3855-3865.

659 Bosak T, Liang B, Wu TD, Templer SP, Evans A, Vali H, Guerquin-Kern JL, Klepac-
660 Ceraj V, Sim, MS, Mui J (2012) Cyanobacterial diversity and activity in modern
661 conical microbialites. Geobiology DOI: 10.1111/j.1472-4669.2012.00334.x
662
663 Burne RV, Moore LS, Christy AG, Troitzsch U, King PL, Carnerup AM,
664 Hamilton PJ (2014) Stevensite in the modern thrombolites of Lake Clifton, Western
665 Australia: A missing link in microbialite mineralization? *Geology* **42**, 575-578.
666
667 Caselmann M (2005) Rezente und subfossile mikrobialithe westaustralischer salzseen.
668 Doctoral Thesis, Georg-August-Universitat zu Gottingen. http://ediss.uni-
669 goettingen.de/handle/11858/00-1735-0000-0006-B32C-0
670
671 Cloud P, Lajoie KR (1980) Calcite-impregnated defluidization structures in littoral
672 sands of Mono Lake, California. *Science* **210**, 1009-1012.
673
674 Council TD, Bennett PC (1993) Geochemistry of ikaite formation at Mono Lake,
675 California: Implications for the origin of tufa mounds. *Geology* **21**, 971-974.
676
677 Couradeau E, Benzerara K, Gerard E, Moreira D, Bernard S, Brown Jr GE, Lopez-
678 Garcia P (2012) An early-branching microbialite cyanobacterium forms intracellular
679 carbonates. *Science* **336**, 459-462.
680
681 Davison W (1993) Iron and manganese in lakes. *Earth-Science Reviews* **34**, 119-163.
682

683 Dekov VM, Egueh NM, Kamenov GD, Bayon G, Lalonde SV, Schmidt M, Liebetrau
684 V, Munnik F, Fouquet Y, Tanimizu M, Awaleh MO, Guirreh I, Le Gall B (2014)
685 Hydrothermal carbonate chimneys from a continental rift (Afar Rift): Mineralogy,
686 geochemistry, and mode of formation. *Chemical Geology* **387**, 87-100.
687
688
689 Della Porta G (2015) Carbonate build-ups in lacustrine, hydrothermal and fluvial
690 settings: comparing depositional geometry, fabric types and geochemical signature.
691 *Geological Society, London, Special Publications* **418**, 17-68.
692
693
694 Drews G, Weckesser J (1982) in: N.G. Carr, B.A. Whitton, (Eds.). *The Biology of*
695 *Cyanobacteria*, Blackwell, London. pp 333-58.
696
697 Dunn JR (1953) The origin of the deposits of tufa in Mono Lake. *Journal of*
698 *Sedimentary Petrology* **23**, 18-23.
699
700 Dupraz C, Fowler A, Tobias C, Visscher PT (2013) Stromatolitic knobs in Storr's
701 Lake (San Salvador, Bahamas): a model system for formation and alteration of
702 laminae. *Geobiology* **11**, 527-548.
703
704 Dupraz C, Reid RP, Braissant O, Decho AW, Norman RS, Visscher PT (2009)
705 Processes of carbonate precipitation in modern microbial mats. *Earth-Science*
706 *Reviews* **96**, 141-162.
707

Dupraz C, Visscher PT, Baumgartner LK, Reid RP (2004) Microbe–mineral interactions: early carbonate precipitation in a hypersaline lake (Eleuthera Island, Bahamas). *Sedimentology* **51**, 745-765.

Emeis KC, Richnow HH, Kempe S (1987) Travertine formation in Plitvice National Park, Yugoslavia: chemical versus biological control. *Sedimentology* **34**, 595-609.

Guo X, Chafetz HS (2012) Large tufa mounds, Searles Lake, California. *Sedimentology* **59**, 1509-1535.

Han J, McCarthy ED, Calvin M, Benn MH (1968) Hydrocarbon consituents of the blue-green algae *Nostoc Muscurum, Anacystis nidulans, Phormidium luridum* and *Chlorogloea fritschii. Journal of the Chemical Society* **1968C**, 2785-2791.

Jennings CW, Strand RG, Rogers TH (1977) Geologic map of California: California Division of Mines and Geology, scale 1:750,000

Jones B, de Ronde CEJ, Renaut RW, Owen RB (2007) Siliceous sublacustrine spring deposits around hydrothermal vents in Lake Taupo, New Zealand. *Journal of the Geological Society of London* **164**, 227-242.

Kazmierczak J, Kempe S, Kremer B, Lopez-Garcia P, Moreira D, Tavera R

730 (2011) Hydrochemistry and microbialites of the alkaline crater lake Alchichica,
731 Mexico. *Facies* **57**, 543-570.

732

733 Kempe S, Kazmierczak J, Landmann G, Konuk T, Reimer A, Lipp A. Largest known
734 microbialites discovered in Lake Van, Turkey. *Nature* **349**, 605-608.

735

736 Konhauser KO, Fyfe WS, Ferris FG, Beveridge TJ (1993) Metal sorption and mineral
737 precipitation by bacteria in two Amazonian river systems: Rio Solimoes and Rio
738 Negro, Brazil. *Geology* **21**, 1103-1106.

739

740 Koning E, Epping E, Van Raphorst W (2002) Determining biogenic silica in marine
741 samples by tracking silicate and aluminium concentrations in alkaline leaching
742 solutions. *Aquatic Geochemistry* **8**, 37-62.

743

744 Kulp TR, Hoeft, SE, Asao, M, Madigan, MT, Hollibaugh, JT, Fisher, JC, Stolz, JF,
745 Culbertson, CW, Miller, LG, Oremland, RS (2008) Arsenic(III) Fuels Anoxygenic
746 Photosynthesis in Hot Spring Biofilms from Mono Lake, California. *Science* **321**,
747 967-970.

748

749 Li HC, Ku TL (1997) $\delta^{13}C$–$\delta^{18}O$ covariance as a paleohydrological indicator for
750 closed-basin lakes. *Palaeogeography, Palaeoclimatology, Palaeoecology* **133**, 69-80.

751

752 Pace A, Bourillot R, Bouton A, Vennin E, Galaup S, Bundeleva I, Patrier P, Dupraz
753 C, Thomazo C, Sansjofre P, Yokoyama Y, Franceschi M, Anguy Y, Pigot L, Virgone

754 A, Visscher PT (2016) Microbial and diagenetic steps leading to the mineralisation of
755 Great Salt Lake microbialites. *Scientific Reports* **6**, 31495.
756
757 Pache M, Reitner J, Arp G (2001) Geochemical Evidence for the Formation of a
758 Large Miocene "Travertine" Mound at a Sublacustrine Spring in a Soda Lake
759 (Wallerstein Castle Rock, N6rdlinger Ries, Germany). *Facies* **45**, 211-230.
760
761 Pedley HM, Rogerson M, Middleton R (2009) Freshwater calcite precipitates from in
762 vitro mesocosm flume experiments: a case for biomediation of tufas. *Sedimentology*
763 **56**, 511-527.
764
765 Petroff AP, Beukes NJ, Rothman DH, Bosak T (2013) Biofilm growth and fossil
766 form. *Physical Review X* **3**, 041012.
767
768 Reid RP, Visscher PT, Decho AW, Stolz JF, Bebout BM, Dupraz C, Macintyre IG,
769 Paerl HW, Pinckney JL, Prufert-Bebout L, Steppe TF, DesMarais DJ (2000) The role
770 of microbes in accretion, lamination and early lithification of modern marine
771 stromatolites. *Nature* **406**, 989-992.
772
773 Rieger T (1992) Calcareous tufa formations. Searles Lake and Mono Lake: California.
774 *Geology* **45**, 99-109.
775
776 Russell IC (1889) Quaternary history of Mono Valley, California. *USGS 8th Annual*
777 *Report for 1886-1887*. p261-394.
778

779 Saunders P, Rogerson M, Wadhawan J, Greenway G, Pedley H (2014) Mg/Ca ratios
780 in freshwater microbial carbonates: Thermodynamic, Kinetic and Vital Effects.
781 *Geochimica et Cosmochimica Acta* **147**, 107-118.
782
783 Scholl DW, Taft WH (1964) Algae, contributors to the formation of calcareous tufa,
784 Mono Lake, California. *Journal of Sedimentary Petrology* **34**, 309-319.
785
786 Shearman DJ, McGugan A, Stein C, Smith AJ (1989) Ikaite, $CaCO_3.6H_20$, precursor
787 of the thinolites in the Quaternary tufas and tufa mounds of the Labontan and Mono
788 Lake basins, western United States. *Geological Society of America Bulletin* **101**, 913-
789 917.
790
791 Shiea J., Brassell SC, Ward DM (1990) Mid-chain branched mono- and dimethyl
792 alkane in hot spring cyanobacterial mats: a direct biogenic source for branched
793 alkanes in ancient sediments? *Organic Geochemistry* **15**, 223–231.
794 Souza-Egipsy V, Wierzchos J, Ascaso C, Nealson KH (2005) Mg-silica precipitation
795 in fossilization mechansims of sand tufa endolithic microbial community, Mono Lake
796 (California). *Chemical Geology* **217**, 77-87.
797
798 Stine S (1987) Mono Lake: The past 4000 years. Unpublished PhD thesis, University
799 of California, Berkley. 614pp.
800
801 Thiel V, Merz-Preiß M, Reitner J, Michaelis W (1997) Biomarker studies on
802 microbial carbonates: Extractable lipids of a calcifying cyanobacterial mat
803 (Everglades, USA). *Facies* **36**, 163–172.

Wacey D, Gleeson D, Kilburn MR (2010) Microbialite taphonomy and biogenicity: new insights from NanoSIMS. *Geobiology* **8**, 403-406.

Wacey D, Kilburn MR, Saunders M, Cliff J, Brasier MD (2011) Microfossils of sulfur metabolizing cells in ~3.4 billion year old rocks of Western Australia. *Nature Geoscience* **4**, 698-702.

Wacey D, Menon S, Green L, Gerstmann D, Kong C, McLoughlin N, Saunders M, Brasier MD (2012) Taphonomy of very ancient microfossils from the ~3400 Ma Strelley Pool Formation and ~1900 Ma Gunflint Formation: new insights using a focused ion beam. *Precambrian Research* **220-221**, 234-250.

Wacey D, Urosevic L, Saunders M, George AD (2017) Mineralization of filamentous cyanobacteria in Lake Thetis stromatolites, Western Australia. *Geobiology* (in press).

Walter MR, Des Marais, DJ (1993). Preservation of biological information in thermal spring deposits: Developing a strategy for the search for fossil life on Mars. *Icarus* **101**, 129-143.

Wang X, Ali G, Hemming SR, Zimmerman SRH, Stine SW, Hemming G (2014) Lake level changes in the Mono Basin during the last deglacial period *American Geophysical Union, Fall Meeting 2014, abstract* **PP51D-1157**

828 Wassenburg J, Scholz D, Jochum KP, Cheng H, Oster J, Immenhauser A, Richter DK,
829 Häger T, Jamieson RA, Baldini JUL, Hoffmann D, Breitenbach SFM (2016)
830 *Geochimica et Cosmochimica Acta* **190**, 347-367.
831
832 Zeyen N, Benzerara K, Li J, Groleau A, Balan E, Robert J-L, Esteve I, Tavera R,
833 Moreira D, Lopez-Garcia P (2015) Formation of low-T hydrated silicates in modern
834 microbialites from Mexico and implications for microbial fossilization. *Frontiers in*
835 *Earth Science* **3**, 64.
836
837 Zimmerman SRH, Hemming SR, Hemming NG, Tomascak PB, Pearl C (2011) High
838 resolution chemostratigraphic record of late Pleistocene lake-level variability, Mono
839 Lake, California. *Geological Society of America Bulletin* **123**, 2320-2334.
840
841
842 **FIGURE CAPTIONS**

This paper is accepted for publication in Geobiology
(https://onlinelibrary.wiley.com/journal/14724669)

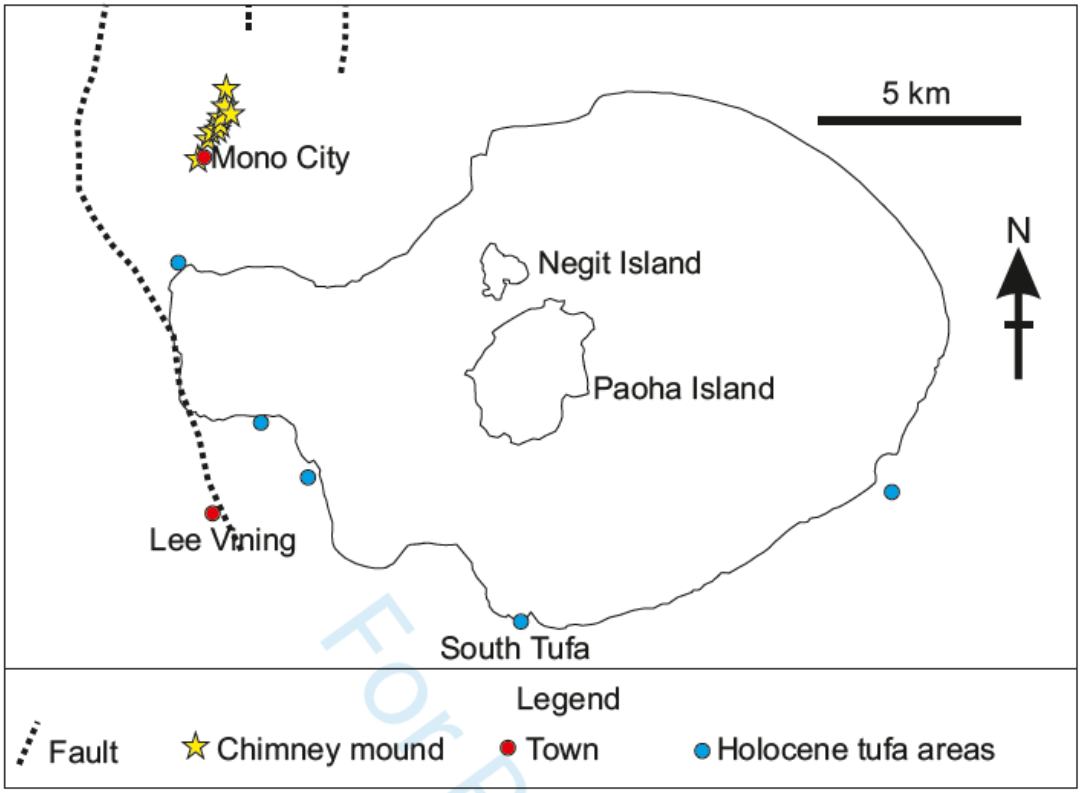

Fig. 1 Map of Mono Lake, California. Pleistocene chimney mounds of the Mono City area described in this article are yellow stars in the northwest corner. Other areas known for the more widely reported Holocene tufa carbonates are shown as blue circles. Towns of Lee Vining and Mono City are shown as red circles. Scale bar is 5 km.

This paper is accepted for publication in Geobiology
(https://onlinelibrary.wiley.com/journal/14724669)

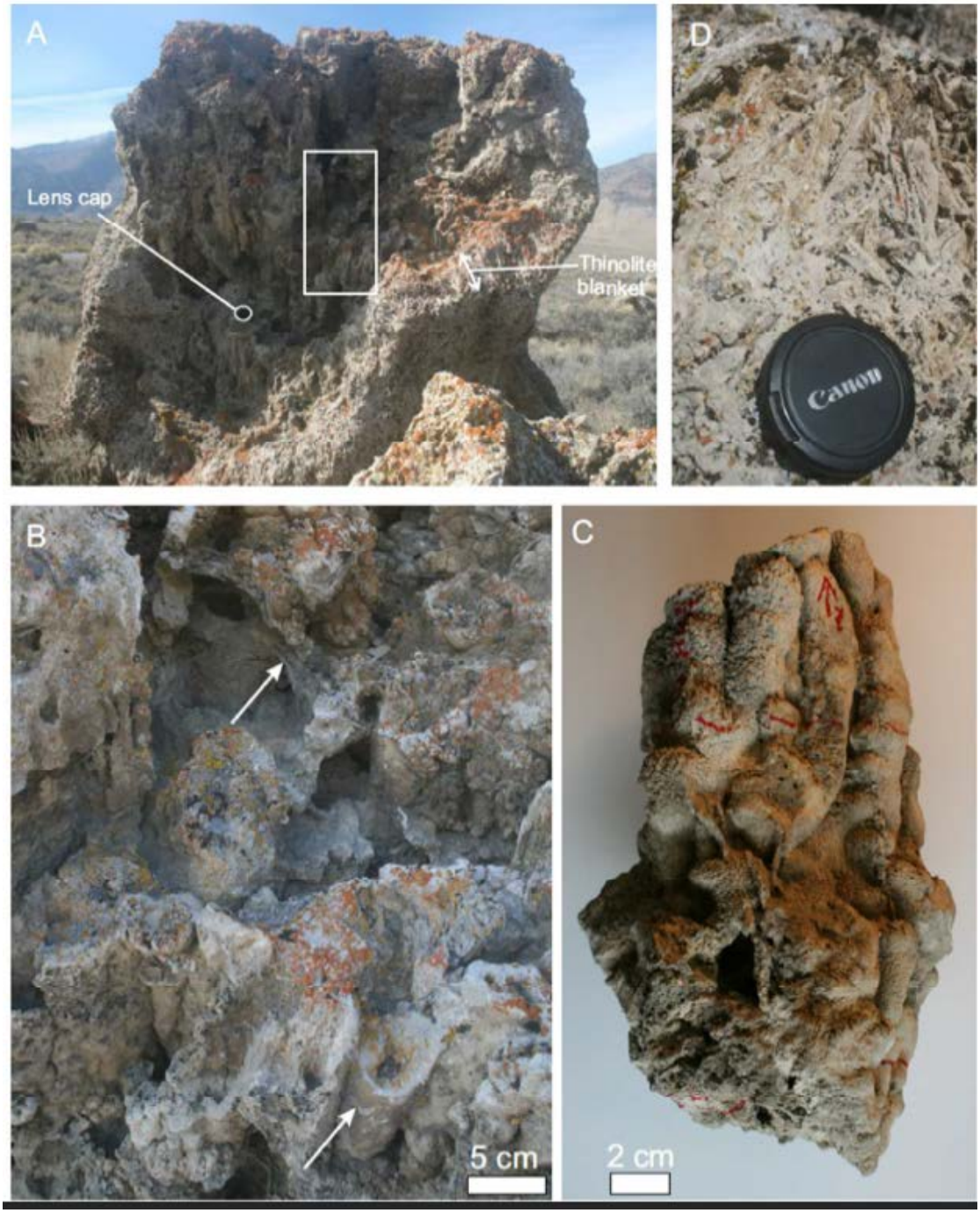

Fig. 2 Field images of Mono City tufa chimneys. (A) One of the chimneys standing erect on former lake floor sediments and coated in a blanket of "thinolite" (pseudomorphs after ikaite, labelled). Lens cap for scale is circled. (B) Close up of pipes in the chimney from the boxed area in (A). Lower arrow points to the exterior of one of the cylindrical pipes that makes up the chimney structure, and upper arrow points to calcitic mat-like structure bridging between pipes. (C) Specimen of pipes on

857 which further micro-scale analyses were undertaken. (D) Close-up of thinolite blanket
858 on the exterior of one of the chimneys, showing these pseudomorphs after ikaite have
859 a very different appearance from the underlying chimney construction illustrated in
860 (B) and (C).
861

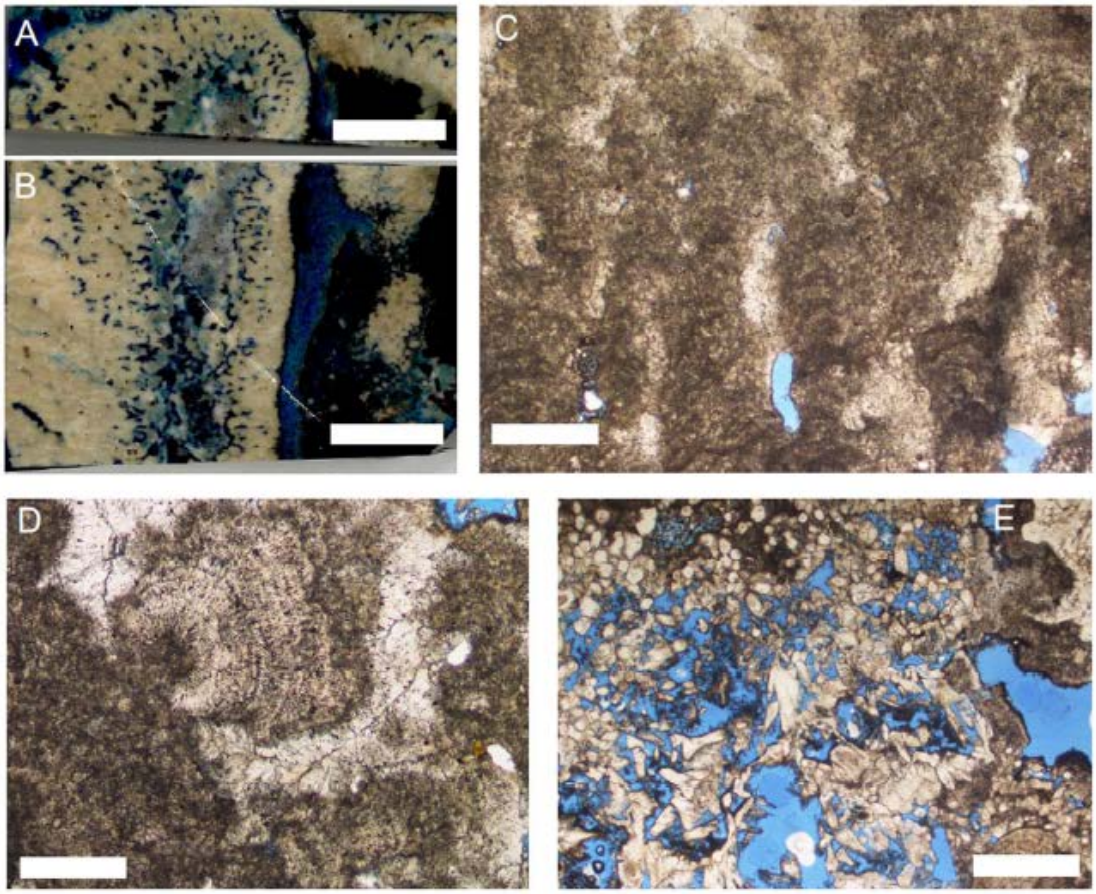

862

863 **Fig. 3** Petrography of Mono City chimneys. (A) Transverse cut and (B) longitudinal
864 cut through one cylindrical chimney pipe. The specimen was impregnated with blue
865 resin, so blue areas were void space in the rock. Axis of the pipe is the (blue resin
866 impregnated) vertical cavity to the left of centre of (B). Space between pipes is also
867 filled with blue resin. (C) Thin-section of pipe wall under plane polarised light
868 showing it comprises columns of laminated micritic calcite separated by partially
869 spar-filled voids (white where spar filled, blue resin where empty). (D) A shrub-like

calcite microspar crystal fan, surrounded by clear white spar and nucleated on darker micrite. The micrite and shrub-like fan in particular are full of dark inclusions (microbial filaments). (E) Inclusion-free crystals best interpreted as pseudomorphs after euhedral ikaite (Shearman et al., 1989), now calcite, are distinctively different from the pipe wall material. The high porosity results from the significant volume change on transformation from ikaite to calcite. Scale bars are 10 mm for (A-B), 1 mm for (C, E) and 500 μm for (D).

This paper is accepted for publication in Geobiology
(https://onlinelibrary.wiley.com/journal/14724669)

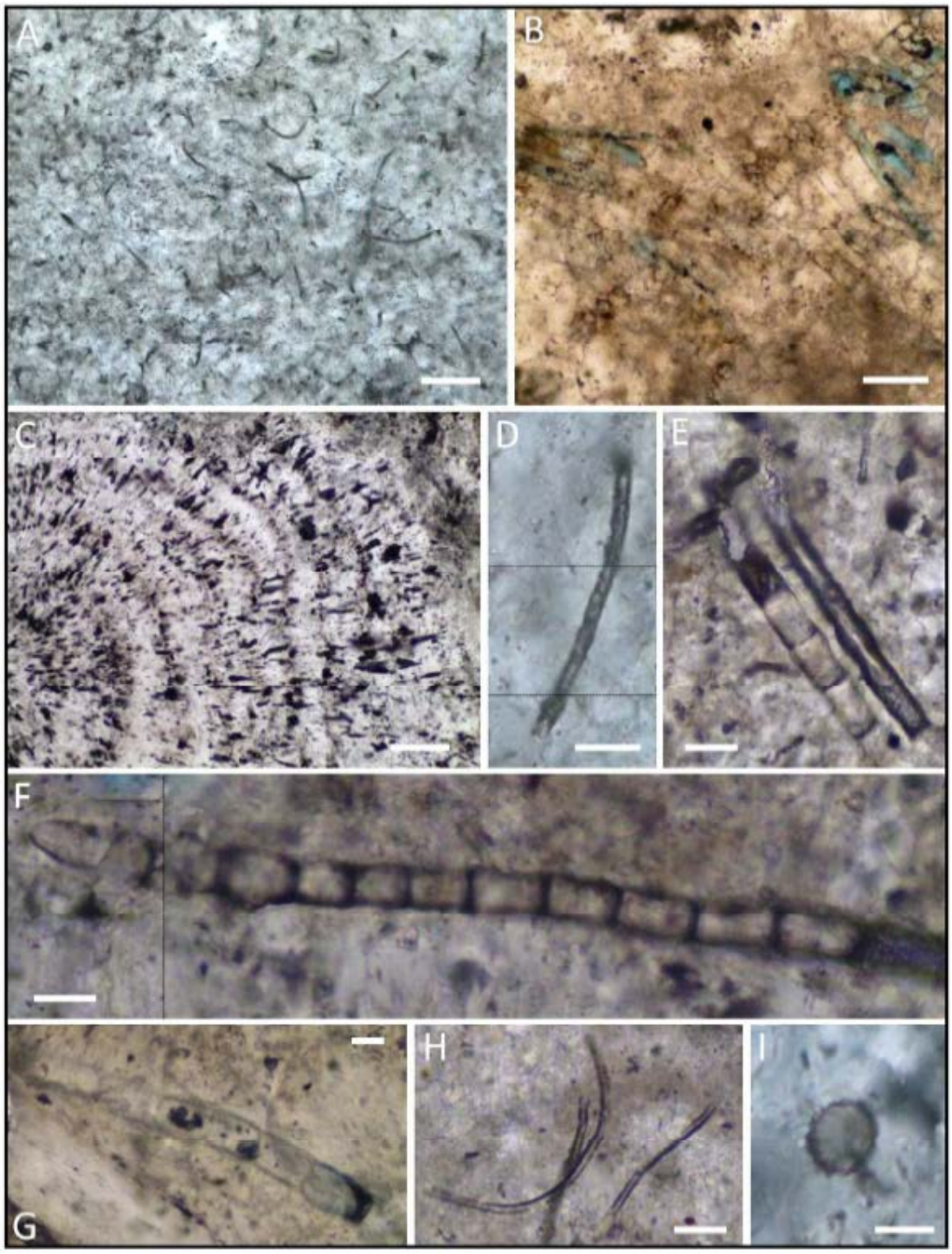

878

879 **Fig. 4** Fossilised bacteria within Mono Lake tufa chimneys. (A) Multiple type 1

880 filaments. (B) Cluster of approximately aligned segmented type 2 filaments. (C) Type

881 1 filaments aligned perpendicular to outward-radiating sub-crystal boundaries. (D)

882 Single Type 1 filament showing putative segmentation. (E) A type 1 and type 2

883 filament side by side. (F) Type 2 filament showing clear segmentation and potentially

partially surrounded by a mineralised sheath. (G) Type 2 filament showing segmentation and potential remnants of cell contents. (H) Typical type 1 empty sheaths. (I) Typical coccoid bacterium. Scale bars are 50 μm for (A-C) and 10 μm for (D-I). Dashed black lines indicate transition between images taken at different focal depths.

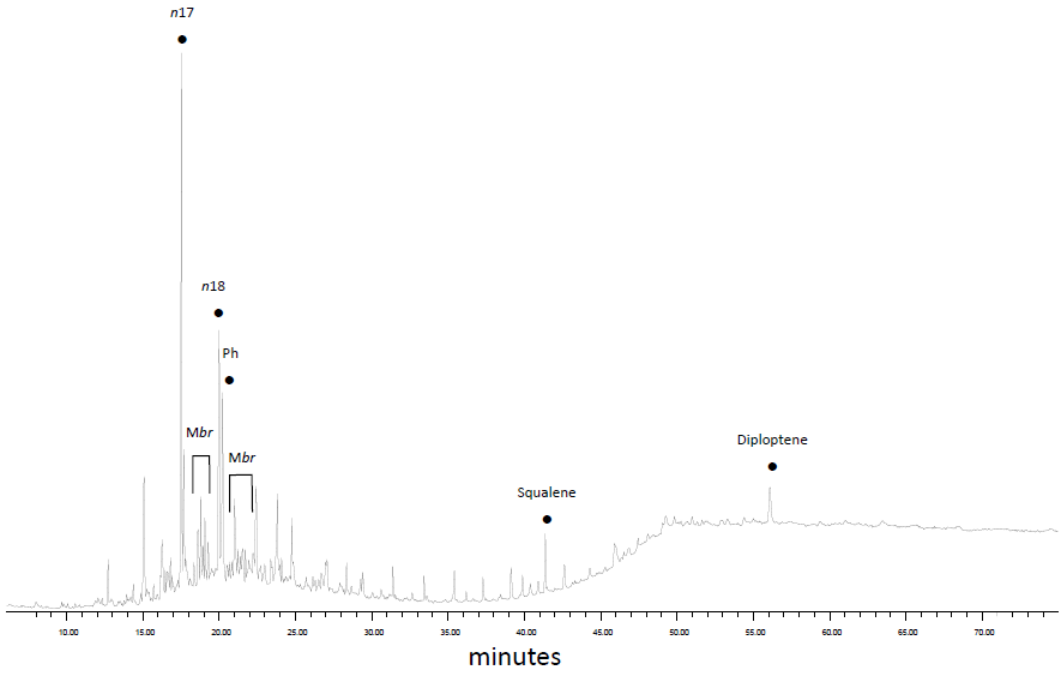

Fig. 5 An 85 + 189 *m/z* ion chromatogram for a Mono City chimney pipe specimen. *n*17 = C_{17} *n*-alkane, Ph = phytane, M*br* = methylbranched alkane. This is consistent with the presence of cyanobacteria entombed within the Mono City chimney pipes.

This paper is accepted for publication in Geobiology
(https://onlinelibrary.wiley.com/journal/14724669)

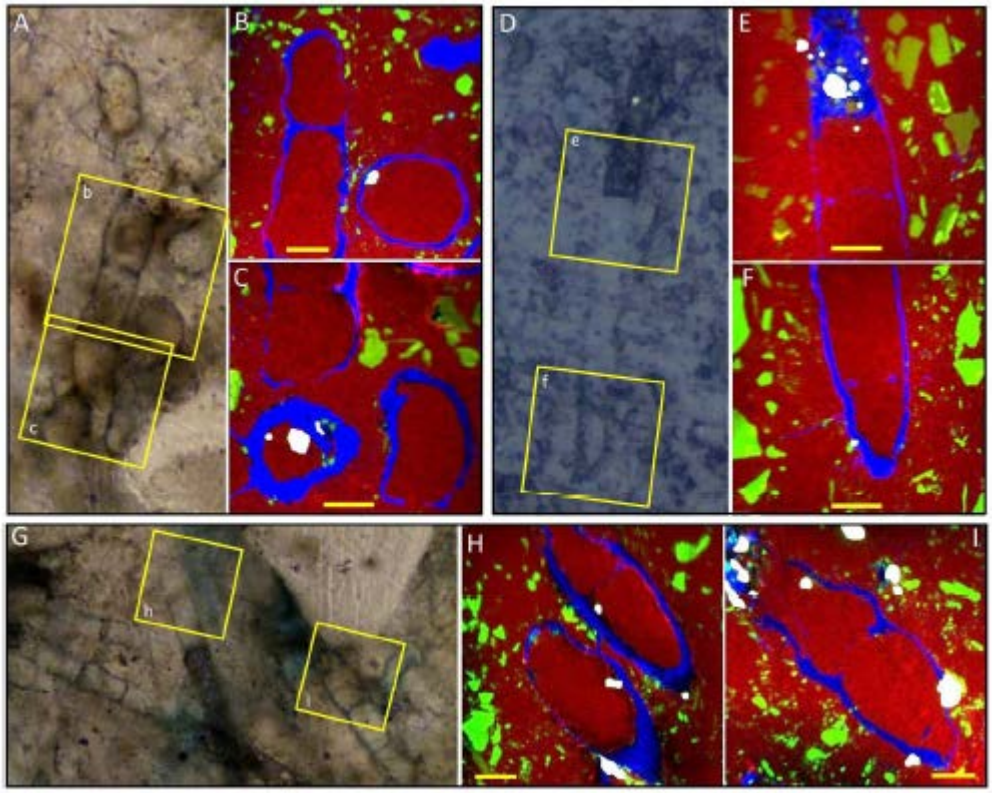

Fig. 6 NanoSIMS analysis of Mono Lake tufa cyanobacteria and associated minerals. Transmitted (A,G) and reflected light (D) images of several segmented filamentous cyanobacteria from a Mono Lake tufa chimney pipe. In each case the areas analysed by NanoSIMS are highlighted by the yellow boxes. (B-C; E-F; H-I) Four colour overlays of NanoSIMS ion images where blue represents organic material, green represents silicate grains, red represents calcite, and white represents contaminant SiC grains from polishing. Silicate grains are found surrounding, but very rarely within, the cyanobacteria. Scale bars are 5 μm for all NanoSIMS images.

This paper is accepted for publication in Geobiology
(https://onlinelibrary.wiley.com/journal/14724669)

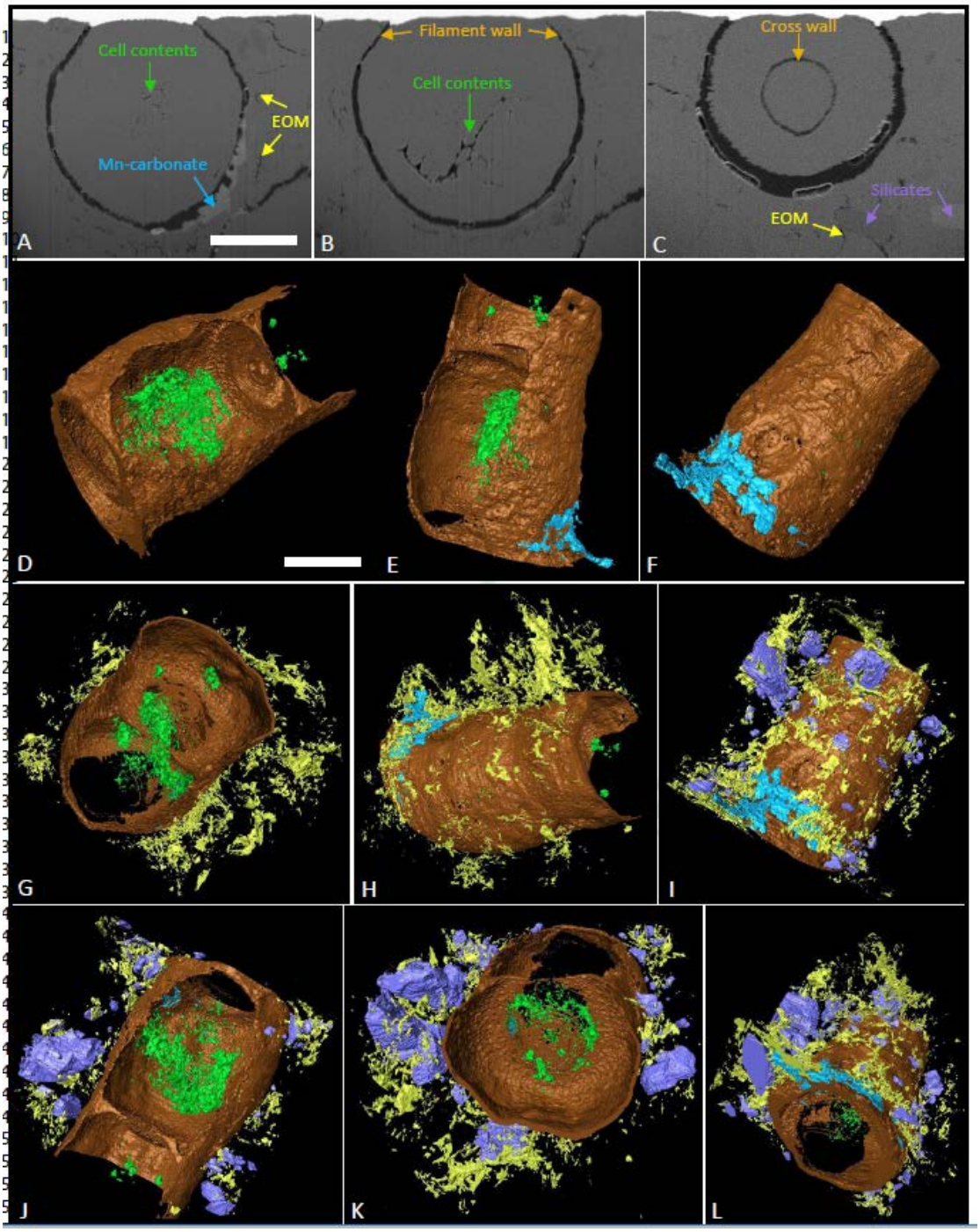

Fig. 7 Three-dimensional analysis of fossilised cyanobacteria from Mono Lake tufa chimney pipes. (A-C) SEM-BSE images of a series of cross sections through a fossilised cyanobacterium. The different components of the cyanobacterium and associated minerals are labelled (based on correlative evidence from EDS and NanoSIMS maps), and the uniform mid-grey material making up most of the field of view is calcite. (D-L) 3D reconstructions of the cyanobacterium and associated

912 minerals. Filament walls and cross walls are shown in brown, organic cell contents in
913 green, inferred extracellular polymeric substances (EOM) in yellow, silicate minerals
914 in purple, and Mn-carbonate in blue. The remainder of each field of view (here made
915 transparent black) is calcite. In reconstructions (D-F) only cell walls, organic cell
916 contents and the Mn-carbonate mineral are shown for clarity; in (G-H) the EOM has
917 been added to the reconstruction; while in (I-L) all components are shown,
918 demonstrating the close spatial association of silicate minerals and EOM. Scale bar in
919 (A) is 5 μm and applies to (A-C), scale bar in (D) is also 5 μm and applies to (D-L).
920

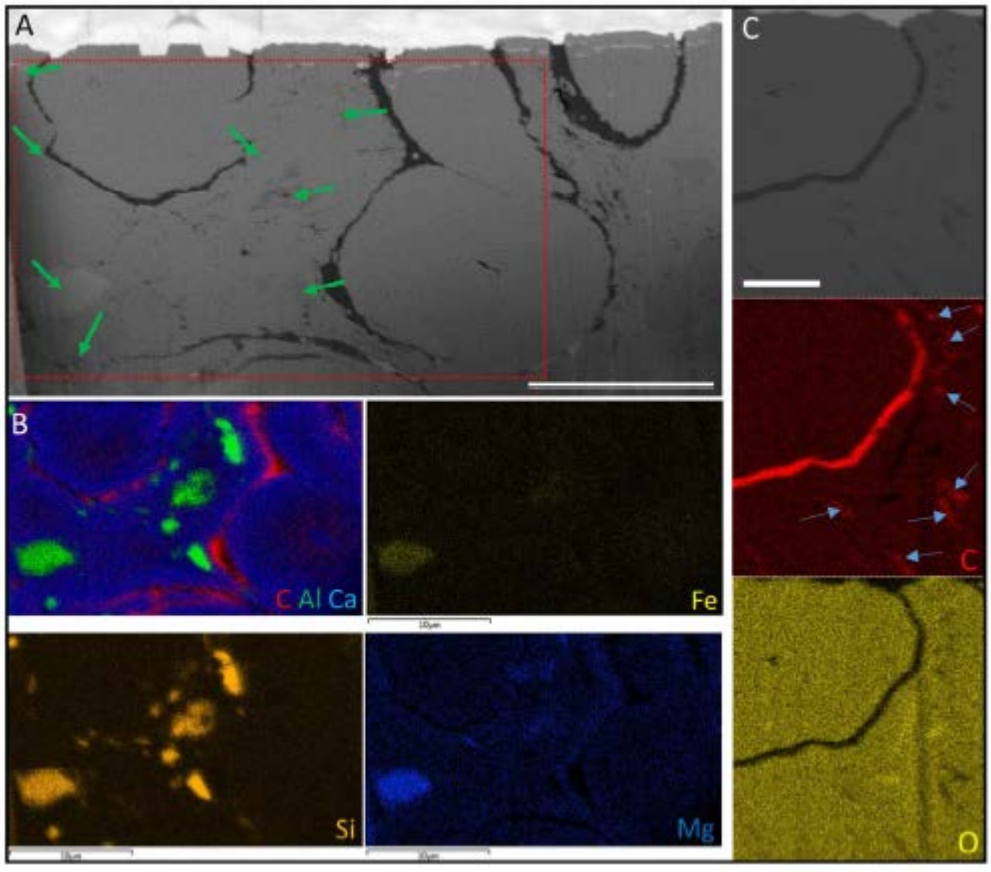

921

922 **Fig. 8** SEM-EDS analysis of the distribution of silicates and organic carbon around
923 Mono Lake tufa cyanobacteria. (A) SEM-BSE image of a cross section through at
924 least three Type 2 cyanobacteria. Note organic cell walls (black) and wispy

925 extracellular organic material (EOM; also black). Red box shows area analysed in (B)
926 and green arrows point to examples of silicates. (B) SEM-EDS elemental maps of
927 carbon, aluminium and calcium (shown as RGB 3 colour overlay), plus iron, silicon
928 and magnesium showing the close association of organic material and various silicate
929 grains. Scale bars are 10 μm. (C) SEM-BSE image of a further Type 2
930 cyanobacterium with SEM-EDS elemental maps of carbon (red) and oxygen (yellow);
931 both the cell wall and the wispy black material seen in the BSE image have elevated
932 carbon contents (arrows) compared to the background carbonate mineral. Scale bar is
933 2 μm.
934

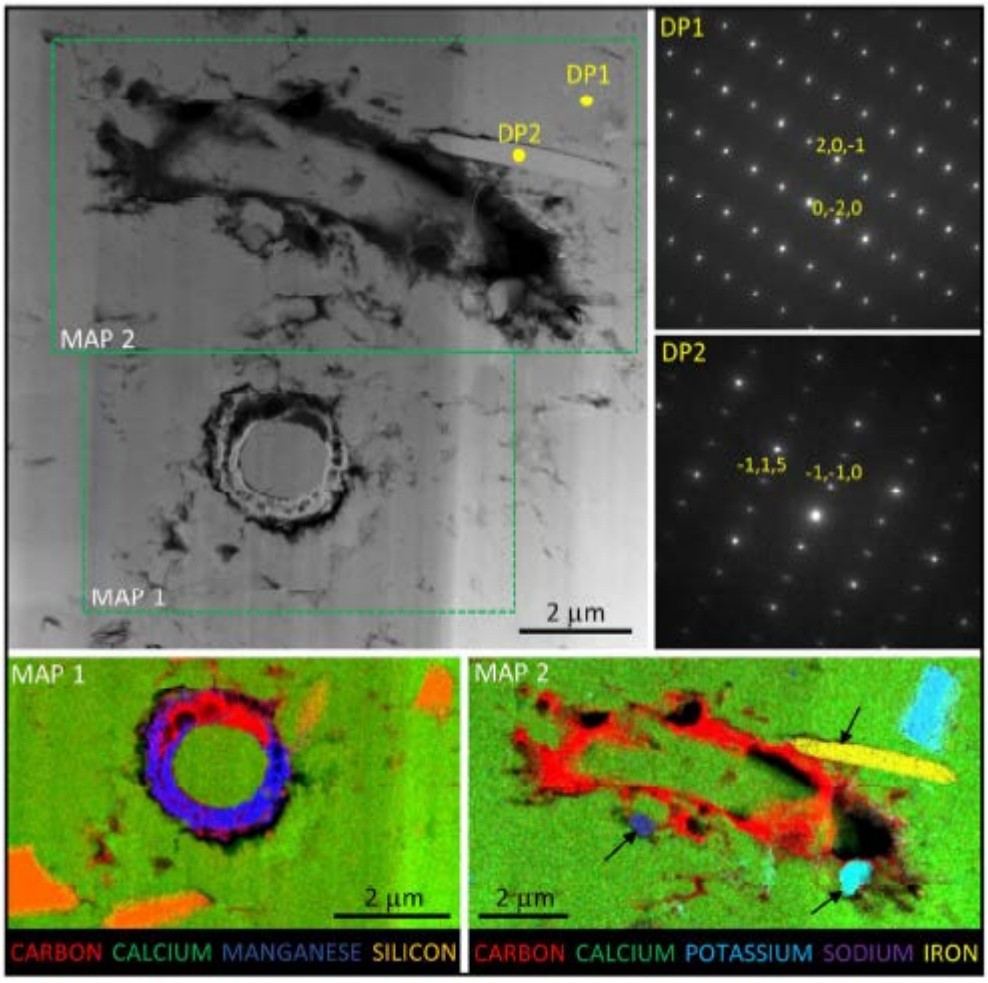

935

936 **Fig. 9** Chemistry of Type 1 filaments and surrounding minerals. High angle annular
937 dark field scanning TEM image showing longitudinal and transverse sections
938 respectively through two Type 1 filaments. The TEM-EDS elemental maps (bottom
939 row) show that the filament walls and some extracellular material retain a
940 carbonaceous composition (red). Some void space is present (black in these elemental
941 maps) and this is not filled with epoxy resin. The lower filament is partly mineralised
942 by an amorphous Mn-rich carbonate (dark blue; also containing minor Ti and Fe).
943 Angular detrital aluminosilicate grains are closely associated with the filaments and
944 some are attached to the outer walls or extracellular organics of the upper filament
945 (black arrows). Aluminosilicate grains are of variable composition with Na-K-rich
946 varieties plus Fe-Mg-rich varieties. Selected area electron diffraction patterns show
947 that the Na-K-rich grains are alkali feldspar (DP1 is consistent with anorthoclase
948 viewed down the [1,0,2] axis), while the Fe-Mg-rich grains are chlorite (DP2 is
949 consistent with clinochlore viewed down the [-5,5,-2] axis).
950

Sample	Al	Ba	Ca	Cu	Fe	K	Li	Mg	Mn	Na	S	Si	Sr
Dechambeau Hot spring	0.019	0.010	11.567	0.002	0.041	6.860	0.232	2.460	0.016	324.789	31.326	18.269	0.162
Lakeside Spring	0.084	0.001	2.238	0.002	0.036	17.584	0.254	0.587	0.001	189.072	17.976	5.272	0.005
Lakewater at island	0.174	0.007	3.316	0.003	0.064	1434.739	11.855	12.861	0.012		1656.138	4.917	0.021
Lakewater at tower	0.046	0.007	3.025	0.004	0.065	1383.753	11.653	12.585	0.011		1704.602	5.092	0.017
Lakewater site 2	0.198	0.008	3.378	0.005	0.066	1461.272	12.069	12.946	0.012		1659.955	4.995	0.021
Lee Vining Creek	0.046	0.011	7.916	0.004	0.124	0.964	0.000	0.565	0.007	2.911	2.171	2.308	0.040
Mill Creek	0.116	0.021	8.526	0.011	0.226	3.466	0.000	0.857	0.011	9.287	3.843	3.093	0.038
Naval Beach spring	0.070	0.372	86.349	0.003	1.178	29.358	2.237	57.634	1.070	305.561	12.326	32.437	0.473
Rush creek	0.025	0.006	6.707	0.002	0.101	0.567	0.000	0.655	0.005	3.056	1.618	2.011	0.030
Simon Spring 2	0.249	0.027	32.969	0.003	0.467	2.442	0.136	18.714	0.064	28.648	2.577	19.282	0.190
Simon Spring 3	0.034	0.016	22.401	0.000	0.045	7.964	0.221	22.580	0.005	40.587	3.974	18.253	0.173
South Tufa lakeside Spring	0.031	0.292	111.943	0.000	8.462	32.005	1.441	45.901	1.994	207.528	15.698	31.001	0.537
Warm spring near Dechambeau	0.075	0.022	17.041	0.003	0.187	2.017	0.000	0.680	0.022	4.892	4.265	1.397	0.052

951

This paper is accepted for publication in Geobiology
(https://onlinelibrary.wiley.com/journal/14724669)

952 **Table 1** –Trace element concentrations of waters found in and around Mono

953 Lake, California in October 2014

954

This paper is accepted for publication in Geobiology
(https://onlinelibrary.wiley.com/journal/14724669)

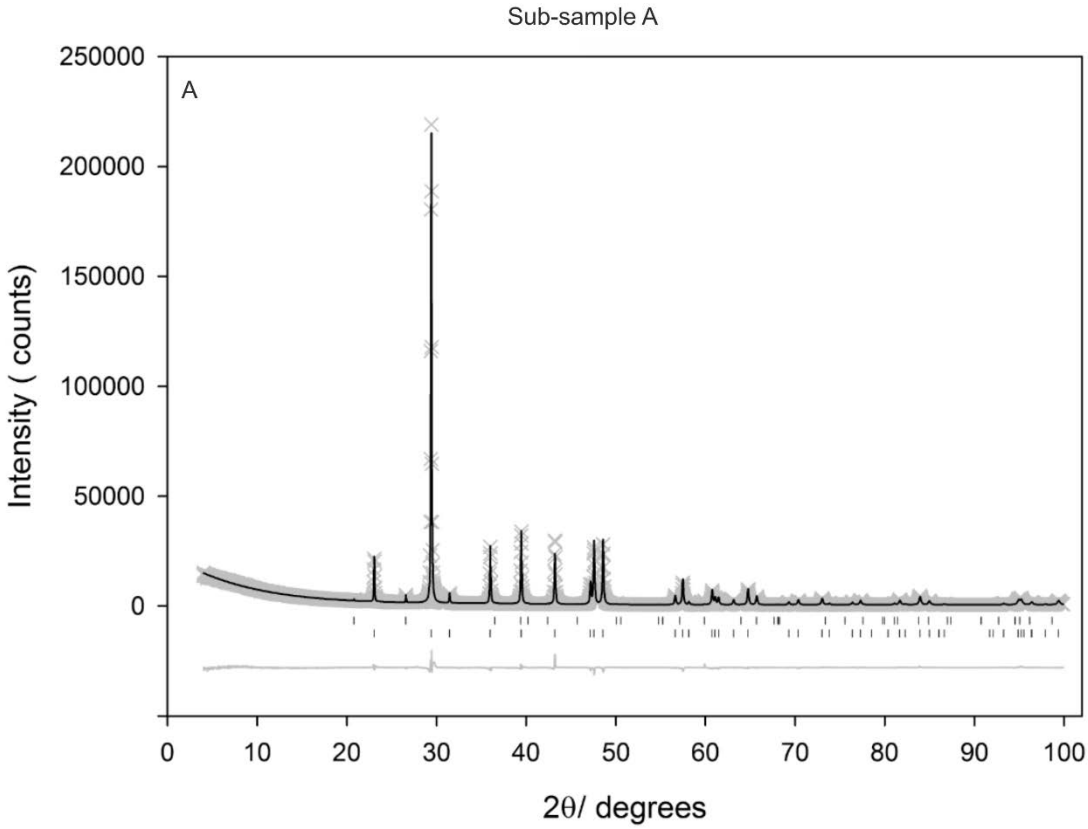

955

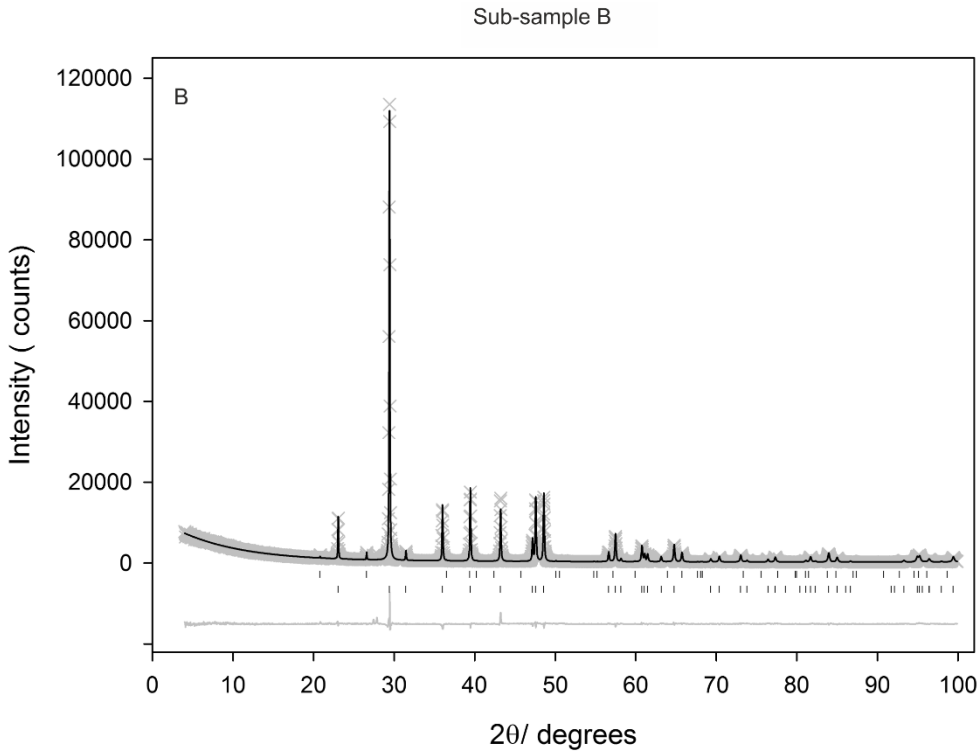

956

This paper is accepted for publication in Geobiology
(https://onlinelibrary.wiley.com/journal/14724669)

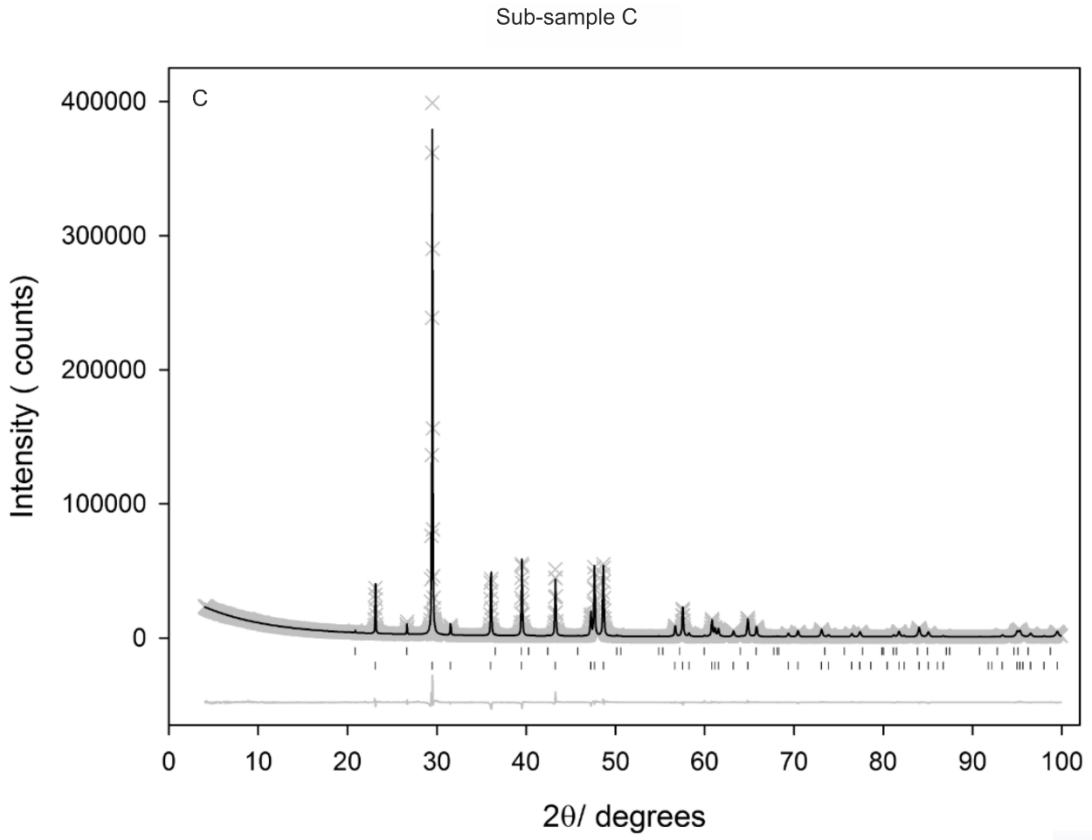

957

958

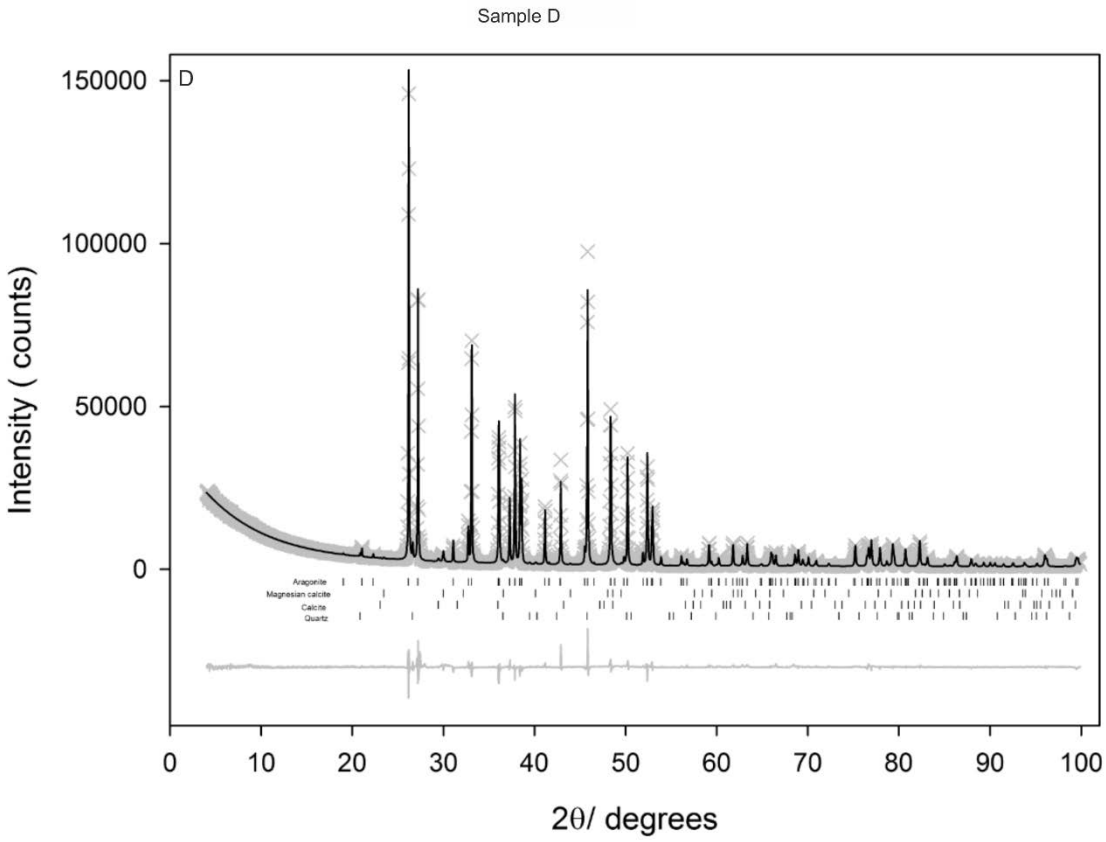

959

This paper is accepted for publication in Geobiology
(https://onlinelibrary.wiley.com/journal/14724669)

960

961 **Fig. S1** Final Rietveld refinement profiles for XRD data from Mono Lake tufa
962 samples. Pleistocene chimney pipe samples (A-C) and Holocene tufa from Lee Vining
963 on the south shore of the modern lake (D) are shown. Plots show observed (grey
964 crosses), calculated (solid black line), and difference (grey line) X-ray powder
965 diffraction profiles for Mono Lake samples at room temperature. The upper tick
966 marks in A, B and C indicate positions of allowed reflections from the $K\alpha_1$ diffraction
967 from silica; the lower set mark allowed reflections from magnesian calcite. The three
968 independent patterns A, B and C are three different sub-samples from the same
969 chimney pipe specimen. Their average composition is 98.99(5) % magnesian calcite,
970 1.01(5)% quartz. The upper tick marks in (D) indicate positions of allowed reflections
971 from the $K\alpha_1$ diffraction from aragonite (highest tick marks); magnesian calcite;
972 calcite; and quartz (lowest tick marks). Holocene tufa from Lee Vining (D) contains
973 the following crystalline constituents by weight:

974 Aragonite 97.15(9) %;

975 Mg-calcite 1.50(11) % (Composition fixed at $Mg_{0.12}Ca_{0.88}CO_3$);

976 Calcite 0.42(4) %;

977 Quartz 0.93(5) %/.

978
979
980
981 **Magnesian calcite** space group R-3m, refined unit cell parameters
982 **Sub-sample A**
983 a = b = 4.97864(7) Å c = 17.0214(3) Å γ = 120° V = 365.382(12) Å^3
984 **Sub-sample B**
985 a = b = 4.97800(6) Å c = 17.0186(3) Å γ = 120° V = 365.228(11) Å^3
986 **Sub-sample C**
987 a = b = 4.97813(5) Å c= 17.0172(2) Å γ = 120° V = 365.216(10) Å^3
988 **Sample D**
989 a = b = 4.9072(14) Å c = 16.678(6) Å γ = 120° V = 347.82(10) Å^3
990
991 **Alpha quartz** space group $P3_221$, refined unit cell parameters

Sub-sample A
a = b = 4.9134(11) Å c = 5.406(2) Å γ = 120° V = 113.03(2) Å^3
Sub-sample B
a = b = 4.9123(11) Å c = 5.408(2) Å γ = 120° V = 113.03(2) Å^3
Sub-sample C
a = b = 4.97813(5) Å c= 5.4056(13) Å γ = 120° V = 113.032(14) Å^3
Sample D.
a = b = 4.9122(14) Å c = 5.406(3) Å γ = 120° V = 112.98(3) Å^3

Aragonite space group Pmcn, refined unit cell parameters
Sample D
a = 4.966617(5) Å b = 7.96480(8) Å c = 5.74961(6) Å V = 227.423(5) Å^3

Calcite space group R-3m, refined unit cell parameters
Sample D
a = b = 4.984(5) Å c = 17.009(19) Å γ = 120° V = 366.0(4) Å^3

(Sub-sample A) Rietveld refinement details
Magnesian calcite 99.13(3)% by weight. (Refined Mg content 7.5(8) %)
Quartz 0.87(3)%
Quality of fit indicators: wRp = 0.0657 R(F^2) = 0.0534

(Sub-sample B) Rietveld refinement details
Magnesian calcite 99.08(3)% by weight. (Refined Mg content 7.4(8) %)
Quartz 0.92(3)%
Quality of fit indicators: wRp = 0.0662 R(F^2) = 0.0502

(Sub-sample C) Rietveld refinement details
Magnesian calcite 98.76(3)% by weight. Refined Mg content 9.4(7) %)
Quartz 1.24(3)%
Quality of fit indicators: wRp = 0.0581 R(F^2) = 0.0506

(Sample D) Rietveld refinement details
Quality of fit indicators: wRp = 0.0579 R(F^2) = 0.0542

$$\mathrm{wRp}=\left\{\frac{\sum w_i(y_i(obs)-y_i(calc))^2}{\sum w_i(y_i(obs))^2}\right\}^{\frac{1}{2}} \text{ and } \mathrm{R}(F^2)=\frac{\sum_{hkl}(F^2_{obs}-F^2_{calc})}{\sum_{hkl}F^2_{obs}}$$

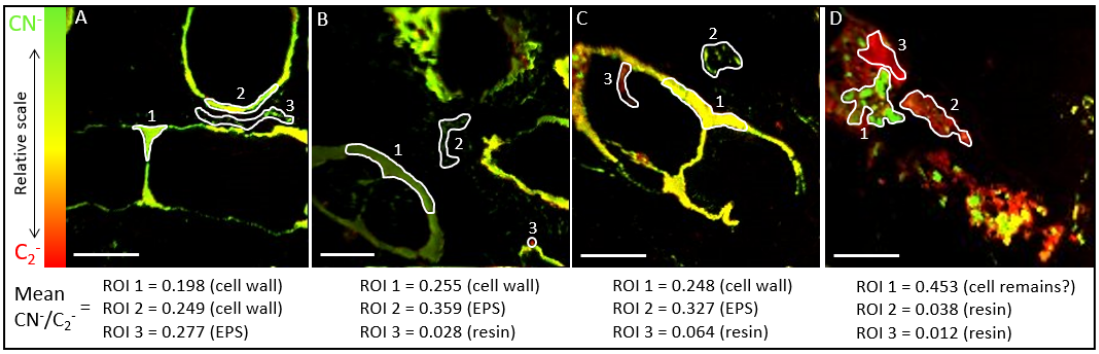

Fig. S2 NanoSIMS CN^-/C_2^- maps demonstrating differential CN^-/C_2^- in cellular and extracellular indigenous organics, plus epoxy resin. (A) Portions of two type 2 filaments (ROI 1 and ROI 2), plus patchy extracellular organics interpreted as EOM (ROI 3) with relatively higher CN^-/C_2^-. (B-C) Examples of Type 2 filaments (ROI 1), patchy EOM (ROI 2), plus zones of porosity within the thin section inferred to be infilled by epoxy resin (ROI 3). Note how the resin has c. 5 to 13 times lower CN^-/C_2^- than the EOM. (D) A degraded type 2 filament that has left a partial hole at the surface of the thin section. The majority of this is infilled by resin with very low CN^-/C_2^- (ROI 2 and 3), while some remnants of the cellular material are also likely present (ROI 1). Note that these maps are not quantitative, so the colour scale only permits comparison of features within the same map, not with features across other maps. Nevertheless, the same pattern emerges in all maps, with epoxy resin having significantly lower CN^-/C_2^- than either the filament walls or the inferred EOM. Scale bars are 5 μm.

This paper is accepted for publication in Geobiology
(https://onlinelibrary.wiley.com/journal/14724669)

1056

1057

1058

1059

1060